The miR-199a-5p/XIAP axis defines cisplatin response, apoptotic control and spatial remodelling in High-grade serous ovarian cancer.

Muñoz-Galdeano, T[1,*†] ; Reigada, D[1]; Nieto-Díaz, M[1]; González Gea, L[2]; García Peña, M.; Palka Kotlowska, M; Santacruz, B[2]; Iglesias, G[3]; M Maza, Rodrigo[1*†]

[1] Molecular Neuroprotection Group, Research Unit, National Hospital for Paraplejics (SESCAM), 45071 Toledo, Spain
[2] Department of Obstetrics and Gynecology, Hospital Universitario de Torrejón, Madrid, Spain.
[3] Department of Informatic Systems, Universidad Politécnica de Madrid, Madrid, Spain.

* Authors to whom correspondence should be addressed.
† These authors contributed equally to this work.

ABSTRACT

High-grade serous ovarian cancer (HGSOC) remains a leading cause of gynecologic cancer mortality, driven largely by late diagnosis and the emergence of platinum resistance. A defining feature of resistant disease is the persistence of pro-survival signaling despite therapeutic stress, frequently converging on blockade of apoptotic execution. XIAP is a central inhibitor of caspase activation, and microRNAs are increasingly recognized as regulators of stress-response networks; however, the functional output of a given miRNA–target relationship can vary with cellular state and treatment context, limiting inference from bulk assays or single-condition measurements.
Here, we interrogate the miR-199a-5p/XIAP axis as an apoptosis-linked regulatory module by integrating (i) evolutionary and structural support for miR-199a-5p engagement with the XIAP 3'UTR, (ii) functional perturbation across paired cisplatin-sensitive and cisplatin-resistant ovarian cancer models, and (iii) spatially resolved validation in human ovarian tissue using multiplex FISH/immunofluorescence. Across cell states, we find that miR-199a-5p does not behave as a fixed "repressor" of XIAP: in the sensitive context, miR-199a-5p is consistent with basal XIAP repression and aligns with facilitated cisplatin-associated apoptotic responses, whereas in the resistant state this coupling is attenuated and cisplatin exposure reshapes the apparent regulatory output, revealing a functional dissociation between XIAP abundance and apoptotic engagement. These observations support context-dependent rewiring of post-transcriptional control during acquired resistance. In FFPE human specimens, multiplex imaging identifies a tumor-associated spatial reorganization of this axis. Non-neoplastic ovary displays compartmental segregation with epithelial-enriched XIAP and relatively weak, stromal-skewed miR-199a-5p, while HGSOC disrupts this architecture with widespread miR-199a-5p, increased spatial convergence with XIAP, and a prominent perinuclear—occasionally nuclear—miR-199a-5p pattern absent from controls, supported by quantitative co-localization descriptors.
Together, our results nominate a human HGSOC-associated spatial phenotype of the miR-199a-5p/XIAP axis and highlight spatially informed strategies for biomarker development and rational resensitization approaches in platinum-resistant disease.

NTRODUCCIÓN

Ovarian cancer lethality is driven less by a lack of initial chemosensitivity than by the near-inevitability of relapse and the clinical challenge of platinum resistance, for which validated predictive or early-state biomarkers remain scarce. Recent clinical syntheses emphasize that platinum resistance is not a single mechanism but a multifactorial, context-dependent phenotype with particularly poor outcomes in primary platinum-resistant disease[1]. At the same time, contemporary biomarker efforts highlight an uncomfortable truth: even when signal exists, it is often missed early enough to matter clinically[2].

A major reason is that resistance is written in space. High-grade serous tumors exhibit pronounced intratumoral heterogeneity, with spatially segregated subclones and microenvironmental niches that can shape drug response and evolutionary trajectories[3]. In parallel, AI-guided spatial profiling work is now showing that clinically relevant "response regions" can be transcriptionally distinct even when conventional histology cannot tell them apart—underscoring the value of spatially resolved molecular readouts in HGSOC[4].

Apoptotic competence is one of the most actionable axes within this landscape. Multiple resistance models converge on attenuation of apoptosis as a key determinant of platinum failure, and inhibitor-of-apoptosis proteins (IAPs) remain central nodes because they can directly buffer caspase activation and intersect survival signaling[5,6]. In ovarian cancer, recent integrative reviews explicitly place XIAP among the anti-apoptotic determinants that may contribute to platinum resistance phenotypes, reinforcing the rationale to interrogate XIAP regulation rather than XIAP abundance alone[5,7].

MicroRNAs provide a mechanistically plausible layer for such context dependence, but most of the field still reads miRNA biology through a "bulk average." Contemporary ovarian cancer reviews continue to highlight miRNA dysregulation as part of the resistance circuitry, yet bulk profiling cannot resolve whether miRNA–target relationships are preserved, redistributed across tumor compartments, or reorganized across subcellular domains[8]. This matters because miRNAs are not strictly cytoplasmic actors: mature miRNAs can localize to the nucleus and participate in gene regulation via multiple mechanisms, expanding the functional space where miRNA signals may operate[9,10].

Within this framework, miR-199a-5p has been implicated as part of tumor-suppressive programs in ovarian cancer and has been linked to recurrence/chemoresistance contexts, including recent work leveraging engineered extracellular vesicles to restore a miR-214-3p/miR-199a-5p network and inhibit chemoresistance-associated phenotypes[11]. Earlier studies also support tumor-suppressive roles for miR-199a-5p in ovarian cancer biology, including microenvironmental settings[12]. Notably, our laboratory previously established that miR-199a-5p acts as a direct repressor of XIAP[13], providing a foundational axis to explore how spatial context influences this interaction in the clinical setting. Together, these reports motivate a focused examination of how miR-199a-5p interfaces with apoptosis control in platinum response.

Here, we investigate whether the miR-199a-5p/XIAP axis contributes to cisplatin response and how this relationship may be altered in resistant states by combining (i) CLIP-informed in silico prediction, (ii) functional interrogation in cisplatin-sensitive and -resistant ovarian cancer cell models, and (iii) spatially resolved miRNA–protein mapping in human FFPE tissue using multiplex miRNA FISH coupled to XIAP immunofluorescence. By integrating mechanism-proximal perturbation with tissue-level spatial organization—including intensity-aware descriptors of miRNA/protein co-distribution—this study positions the miR-199a-5p/XIAP relationship not as another "expression correlation," but as a regulatory architecture whose spatial context may be critical for interpreting platinum resistance phenotypes.

MATERIALS AND METHODS

Análisis in silico de interacción miRNA–mRNA

The accessibility of the miR-199a-5p binding site within the human XIAP 3' untranslated region (3'UTR-XIAP) was assessed using the STarMir prediction platform[14], which applies logistic regression models trained on high-throughput crosslinking immunoprecipitation (CLIP) datasets. Analyses were performed via the STarMir web interface (https://sfold.wadsworth.org/cgi-bin/starmirtest2.pl; accessed on 5 November 2022). The mature hsa-miR-199a-5p sequence was entered under "microRNA sequence(s), microRNA ID(s)", while the human XIAP 3'UTR sequence was provided through the "single target sequence, manual sequence entry" field. The model was configured with the parameters "V-CLIP based model (human)", "Human (Homo sapiens)", and "3'UTR". Output parameters—detailed in the STarMir manual (http://sfold.wadsworth.org/data/STarMir_manual.pdf; accessed on 5 November 2021)—included hybridization energy (ΔG_hybrid), seed-pairing configuration, site accessibility scores, and the composite LogitProb value estimating the probability of functional binding. Complementarily, the local RNA secondary structure encompassing the predicted miR-199a-5p target site was modeled using RNAfold (ViennaRNA Package). This analysis enabled visualization of the base-pairing architecture and estimation of the thermodynamic accessibility of the target region, key determinants of miRNA–mRNA hybridization. Both human and murine XIAP 3'UTR sequences were folded under identical conditions to evaluate the evolutionary conservation of structural features surrounding the binding site. The resulting centroid and minimum free-energy (MFE) structures were inspected to confirm that the predicted seed-matching region remained structurally exposed and energetically favorable for miR-199a-5p binding.

Description of Patient Samples and RNA Isolation from Paraffin Samples and Cell culture

Formalin-fixed paraffin-embedded (FFPE) ovarian tissue samples were obtained from the Department of Gynecology and Obstetrics of the Hospital Universitario de Torrejón de Ardoz (Madrid, Spain). The study included ten high-grade serous ovarian carcinoma (HGSOC) samples and ten non-neoplastic control tissues derived from oophorectomy or

hysterectomy procedures performed for benign gynecological conditions. Representative hematoxylin and eosin (H&E)-stained sections from each block were reviewed by a qualified pathologist to confirm the histopathological diagnosis. For each FFPE tissue block, a 3 mm punch biopsy was obtained from the selected region of interest (tumor or control). All specimens were anonymized and numerically coded prior to analysis, and the codes were blinded to the investigators to minimize experimental bias.

Human ovarian carcinoma cell lines A2780 (ECACC 93112519; RRID:CVCL_0134) and its cisplatin-resistant derivative A2780cis (ECACC 93112517; RRID:CVCL_0135) were purchased from the Cell Bank of the Centro de Instrumentación Científica (CIC), University of Granada (Spain). Both cell lines were supplied certified free of bacterial, fungal, and mycoplasma contamination and authenticated by short tandem repeat (STR) profiling by the CIC-UGR Cell Bank, ensuring compliance with all standard quality control parameters. Both lines display epithelial morphology and were cultured under biosafety level 2 conditions in accordance with ACDP guidelines. A2780 cells were maintained in RPMI-1640 medium (Gibco) supplemented with 2 mM L-glutamine and 10% fetal bovine serum (FBS; Gibco). A2780cis cells were cultured in the same basal medium containing 2 mM L-glutamine, 10% FBS, and 1 μM cisplatin to preserve the resistant phenotype. For subculturing, confluent monolayers (70–80%) were detached with 0.25% trypsin-EDTA and reseeded at ratios of 1:3–1:6 for A2780 and 1:5–1:20 for A2780cis. After thawing, A2780cis cells were initially recovered in cisplatin-free medium for 24–48 h prior to re-exposure to the drug. Cells were maintained at 37 °C in a humidified incubator with 5% CO_2.

Transfection and drug treatment

Transient transfections were performed according to the manufacturer's instructions for DharmaFECT-4 reagent (Dharmacon, Horizon Discovery; Waterbeach, UK). Cells were transfected for 24 h with 50 nM miRIDIAN hsa-miR-199a-5p mimic (miRBase accession number MIMAT0000231; Dharmacon cat. no. C-300533-03-0002, mature sequence: 5′-CCCAGUGUUCAGACUCCUGUUC-3′) or a non-targeting negative control mimic derived from Caenorhabditis elegans (cel-miR-67-3p, miRBase accession number MIMAT0000039; Dharmacon cat. no. CN-001000-01-05, mature sequence: 5′-UCACAACCUCCUAGAAAGAGUAGA-3′). The control mimic exhibits minimal sequence identity to any known human, mouse, or rat miRNA and was used to account for non-specific transfection effects. Where applicable, following transfection, cultures were treated with 12.5 μM cisplatin (cis-diamminedichloroplatinum II; Sigma-Aldrich, cat. no. P4394) for 24 h under standard incubation conditions. Control groups were handled in parallel and exposed to cisplatin-free medium to ensure identical experimental timelines across all conditions.

RNA extraction and quantitative PCR (RT-qPCR)

Basal expression levels of XIAP mRNA and miR-199a-5p were assessed in A2780 and A2780cis ovarian carcinoma cells under untreated conditions. Confluent cultures were harvested, and total RNA was extracted using QIAzol Lysis Reagent (Qiagen; Cat. No. 79306) followed by purification with the miRNeasy Mini Kit (Qiagen; Cat. No. 217004), according to the manufacturer's instructions. RNA concentration and purity were determined using a NanoDrop ND-1000 spectrophotometer (Thermo Fisher Scientific). For miR-199a-5p quantification, 10 ng of total RNA were reverse-transcribed and amplified using a TaqMan MicroRNA-specific probe (TaqMan® MicroRNA Assay #000498, Applied Biosystems; Foster City, CA, USA) following the manufacturer's protocol. The U6 small nuclear RNA served as an internal control (TaqMan® MicroRNA Assay #001973, Applied Biosystems). For XIAP mRNA quantification, 1 µg of total RNA was treated with DNase I (Roche; Cat. No. 10104159001) for 30 min at 37 °C and 3 min at 95 °C, followed by reverse transcription using Moloney murine leukemia virus reverse transcriptase (M-MLV; Invitrogen, Thermo Fisher Scientific; Cat. No. 28025013) and a random primer mix (Roche; Cat. No. 48190011) for 60 min at 37 °C and 3 min at 95 °C. Quantitative PCR was performed using the TaqMan Universal PCR Master Mix (no AmpErase UNG) (Applied Biosystems, Thermo Fisher Scientific; Cat. No. 4324020) together with the corresponding FAM-MBG–conjugated probes for XIAP mRNA (Life Technologies; cat. no. 4331182; Hs00180269_m1) and miR-199a-5p (Applied Biosystems; cat. no. 000498). 18S rRNA (Life Technologies; cat. no. 4333760; Hs99999901_s1) and U6 RNA (Applied Biosystems; cat. no. 001973) were used as endogenous controls for mRNA and miRNA normalization, respectively. Amplification was carried out on a TaqMan 7900HT Fast Real-Time PCR System (Applied Biosystems) under the 9600 emulation mode (10 min at 95 °C, followed by 40 cycles of 15 s at 95 °C and 1 min at 60 °C). Relative expression levels were calculated using the $2^{-\Delta\Delta Ct}$ method (Livak and Schmittgen, 2001), with error propagation performed according to Headrick et al. (2008). Results were expressed as fold changes in A2780cis relative to A2780, including 95% confidence intervals.

Protein extraction and Immunoblotting

For protein expression analyses, A2780 and A2780cis ovarian carcinoma cells were cultured in 6-well plates (2.5×10^5 cells per well) until approximately 80% confluence. Depending on the experimental condition, cultures were either left untreated (for basal XIAP expression) or subjected to transfection with miR-199a-5p or negative control mimics for 24 h, followed—where indicated—by treatment with 12.5 µM cisplatin for an additional 24 h. Cells were harvested by mechanical detachment and lysed in RIPA buffer (Thermo Fisher Scientific; Cat. No. 89900) supplemented with cOmplete™ EDTA-free protease inhibitor cocktail (Merck; Cat. No. 11873580001), incubated for 30 min at 4 °C, and cleared by centrifugation at 12 000 × g for 10 min at 4 °C. Protein concentration was determined using the Pierce™ BCA Protein Assay Kit (Thermo Fisher Scientific; Cat. No. 23225) according to the manufacturer's protocol. Equal protein amounts were mixed with Laemmli sample buffer (Bio-Rad; Cat. No. 1610747) containing β-mercaptoethanol (Sigma-Aldrich; Cat. No. M6250), bromophenol blue (Sigma-Aldrich; Cat. No. B8026),

SDS (Sigma-Aldrich; Cat. No. L3771), and 62.5 mM Tris–HCl (pH 6.8), and boiled for 5 min at 100 °C. After SDS-polyacrylamide gel electrophoresis (SDS-PAGE), proteins were transferred onto Immobilon-P PVDF membranes (0.2 μm pore size; Merck Millipore; Cat. No. IPVH00005). Membranes were blocked for 1 h at room temperature in 5% non-fat dry milk (Nestlé Skim Milk) diluted in TBS-T buffer (Tris-buffered saline, Fisher Scientific; Cat. No. BP2471, plus 0.05% Tween-20; Merck; Cat. No. P1379) and incubated overnight at 4 °C with the appropriate primary antibodies diluted in blocking solution. After washing, membranes were incubated for 90 min at room temperature with HRP-conjugated secondary antibodies (For detailed information regarding the primary and secondary antibodies used, see Table 1). Protein bands were detected using the SuperSignal™ West Pico PLUS Chemiluminescent Substrate (Thermo Fisher Scientific; Cat. No. 34580) and visualized with an ImageScanner III and LabScan v6.0 software (GE Healthcare Bio-Sciences AB, Chicago, IL, USA). Band intensities were quantified using ImageJ v1.54p (NIH, Bethesda, MD, USA). All antibodies recognized specific bands corresponding to the expected molecular weight of their targets without cross-reactivity or non-specific signal.

Table 1. Primary and secondary antibodies used in this study

Antibody	Reference
Primary antibodies for Immunoblot	
anti-XIAP	BD Biosciences (Franklin Lakes, NJ, USA) Cat# 610716, RRID:AB_398039)
anti-β-Actin	BD Biosciences (Franklin Lakes, NJ, USA); Cat# 612656, RRID:AB_2289199
Primary antibodies for Immunofluorescence	
anti-XIAP	(Abcam Cat# ab21278, RRID:AB_446157)
anti-Caspase 3 fragment	(Cell Signaling Technology Cat# 94530, RRID:AB_3076239)
Primary antibody for FISH	
Alkaline phosphatase–conjugated sheep anti-digoxigenin	Sigma-Aldrich Cat# 11093274910, RRID:AB_2734716
Secondary antibodies for Immunoblot	
HRP-conjugated goat anti-rabbit	Cell Signaling Technology (Danvers, MA, USA); Cat# 7074, RRID:AB_2099233
HRP-conjugated goat anti-mouse	Cell Signaling Technology; Cat# 7076, RRID:AB_330924
Secondary antibodies for Immunofluorescence	
Alexa Fluor 488 goat anti-mouse, highly cross-adsorbed	Molecular Probes (Eugene, OR, USA); Cat# A11029, RRID:AB_138404

Fluorescence in situ hybridization (FISH)

FISH in human ovarian tissue (FFPE samples). FISH detection of miR-199a-5p was performed on formalin-fixed paraffin-embedded (FFPE) human ovarian tissue sections, including healthy ovarian samples and high-grade serous ovarian carcinoma (HGSOC), following an adaptation of the protocol described by Søe et al.[15]. All solutions were prepared with DEPC-treated water (1:1000; Merck KGaA, Darmstadt, Germany). Slides were first incubated at 65 °C for 2 h in a dry oven to promote tissue adhesion, followed

by deparaffinization in xylene at room temperature (15 min × 2) and graded rehydration in ethanol (100%: 2 min × 2; 80%: 2 min; 70%: 2 min) before immersion in distilled water. Antigen retrieval was performed by incubating the slides in 250 mM EDTA preheated to 97 °C in a PT Link system (Agilent Technologies, Santa Clara, CA, USA) for 20 min, followed by a distilled water rinse. Enzymatic digestion was carried out by applying Pepsin Solution (ZytoVision, Bremerhaven, Germany) to each section and incubating the slides in a humidified chamber at 37 °C for 30 min, followed by a 5-min wash in PBS 1×. Hybridization was performed by adding DIG-labeled LNA probes specific for miR-199a-5p or the negative control cel-miR-67 (Eurogentec, Seraing, Belgium) to each section, denaturing at 85 °C for 15 min and hybridizing overnight at 37 °C. After 24 h, slides were washed in a hybridization oven at 75 °C with 0.4× SSC containing 0.3% NP-40 (2 min) and 0.2× SSC with 0.1% NP-40 (1 min at room temperature). Sections were then blocked for 15 min at 37 °C in 5% horse serum and 1% BSA in PBS-T-DEPC, followed by incubation with an alkaline phosphatase–conjugated anti-digoxigenin antibody (see Table 1) for 20 min at 37 °C. Signal detection was performed using the Vector Blue Alkaline Phosphatase Substrate Kit (Vector Laboratories, Newark, CA, USA) according to the manufacturer's instructions. Images of stained sections of the human ovarian tissue were taken using a fully motorized Olympus IX83 microscope (Olympus, Tokio, Japan) equipped with Cell Sense Dimensions software V4.1.1 (Olympus).

FISH in cultured ovarian cancer cells (A2780 and A2780cis). FISH analysis of miR-199a-5p was performed in A2780 and A2780cis ovarian carcinoma cells grown on sterile glass coverslips, following an adapted protocol optimized for DIG-labeled LNA probes (Eurogentec, Seraing, Belgium) under RNase-free conditions. All solutions were prepared with DEPC-treated water (1:1000; Merck KGaA, Darmstadt, Germany) and all steps were conducted under RNase-free conditions. Cells were washed twice with PBS-DEPC and permeabilized with PBS containing 0.1% Tween-20 (PBS-T) for 15 min at room temperature. Acetylation was then performed using freshly prepared buffer composed of H_2O-DEPC (98.3%), triethanolamine (1.3%), HCl (0.06%), and acetic anhydride (0.25%, added immediately before use). Samples were incubated for 10 min at room temperature and washed for 5 min in PBS-DEPC. For hybridization, cells were preincubated for 30 min at 65 °C in a 1:1 mixture of Exiqon miRCURY LNA hybridization buffer and DEPC-H_2O, then incubated for 1 h at 65 °C with DIG-labeled LNA probes specific for miR-199a-5p or the negative control cel-miR-67, diluted 1:100 (final ≈200 nM). Probes were denatured at 80 °C for 5 min immediately before use. Post-hybridization washes were performed sequentially in 5× SSC (3 min at 65 °C), 1× SSC (3 min at 65 °C), 0.1× SSC (3 min at 65 °C), and 0.1× SSC (3 min at room temperature). Cells were then blocked for 15 min at 37 °C in 2% horse serum and 1% BSA in PBS-T. Detection of the hybridized probe was achieved using an anti-digoxigenin antibody conjugated to alkaline phosphatase, followed by chromogenic development with the Vector Blue Alkaline Phosphatase Substrate Kit according to the manufacturer's instructions. Preparations were imaged in an epifluorescence microscope (DM5000B, Leica Microsystem GmbH; Wetzlar, Germany) with a 20× objective obtaining 5 images per sample. No XIAP staining was detected in controls without primary antibodies.

Table 2. Sequences of the probes used for miR-199-5p detection by FISH. Oligonucleotides probe sequences complementary to miR-199a-5p and negative control mimics with no complementary targets. Probes are composed of the combination of 2′-O-methyl ([]) and LNA ({}) nucleotides designed following the method from Søe et al.)

Probe	Sequence
Negative Control	5′-DIG-{G}[T]{GU}[A]{AC}[A]{CG}[T]{CU}[A]{UA}[C]{GC}[C]{CA}-3′
miR-199a-5p	5′-DIG-{G}[AA]{C}[AG]{G}[UA]{G}[UC]{T}[GA]{A}[CA]{C}[UG]{GG}-3′

Cell Death Assays

MTT Cell Viability Assay

Cell viability was determined using the 3-(4,5-dimethylthiazol-2-yl)-2,5-diphenyltetrazolium bromide (MTT) colorimetric assay as an index of mitochondrial metabolic activity. A2780 and A2780cis ovarian carcinoma cells were seeded in transparent 96-well plates at a density of 2×10^4 cells/well and allowed to adhere overnight. Transfection and treatment were performed as described above, using miR-199a-5p or negative control mimics, followed by 12.5 μM cisplatin or vehicle exposure for 24 h under standard culture conditions.

After treatment, MTT reagent (Merck KGaA, Darmstadt, Germany; cat. no. M5655) was added directly to the culture medium at a final concentration of 0.5 mg/mL, and cells were incubated for 3 h at 37 °C protected from light. The resulting formazan crystals were solubilized by adding 100 μL of an HCl:isopropanol solution (1:500; Merck KGaA) to each well. Absorbance was measured at 570 nm, with 660 nm used for background correction, using a Tecan Infinite M200 Pro microplate reader (Tecan Group Ltd., Männedorf, Switzerland). Cell viability was expressed as normalized absorbance values relative to the untreated negative control condition.

Propidium Iodide (PI) Staining Assay

Late cell death was evaluated by assessing plasma membrane integrity through propidium iodide (PI) staining. After transfection and treatment as described above, A2780 and A2780cis ovarian carcinoma cells cultured on sterile glass coverslips were incubated for 30 min at 37 °C in warm phosphate-buffered saline (PBS) containing 0.4 μg/mL propidium iodide (Sigma-Aldrich; cat. no. P4170), protected from light. Following incubation, cells were washed twice with PBS and mounted using DAKO Fluorescence Mounting Medium (Agilent Technologies; cat. no. S3023). Fluorescence images were acquired using an epifluorescence microscope (DM5000B, Leica Microsystems GmbH; Wetzlar, Germany) equipped with a 20x objective and a Leica DFC 3000 G digital camera. The percentage of PI-positive cells relative to the total nuclei count was used as an index of late, irreversible cell death.

Caspase-3/7 Activity Assay

Effector caspase activity was analyzed at the single-cell level using the CellEvent™ Caspase-3/7 Green Detection Reagent (Thermo Fisher Scientific; cat. no. C10423), which enables fluorescent detection of apoptotic cells through cleavage of the DEVD peptide sequence. After transfection and treatment as described above, A2780 and A2780cis ovarian carcinoma cells grown on sterile glass coverslips were incubated for 30 min at 37 °C in warm phosphate-buffered saline (PBS) supplemented with 2.5 μM CellEvent™ reagent and 10% fetal bovine serum, protected from light.

Following incubation, the reagent was removed and cells were fixed with 4% paraformaldehyde (PFA) for 15 min at room temperature, then washed three times for 5 min each with PBS 1×. During the first wash, nuclei were counterstained with DAPI (Thermo Fisher Scientific; cat. no. D1306). After washing, samples were mounted using DAKO Fluorescence Mounting Medium (Agilent Technologies; cat. no. S3023). Fluorescence images were acquired using an epifluorescence microscope (DM5000B, Leica Microsystems GmbH; Wetzlar, Germany) equipped with a 20x objective and a Leica DFC 3000 G digital camera. Green fluorescence identifies cells with active caspase-3/7, indicating early apoptosis, while DAPI allowed nuclear visualization. The proportion of caspase-positive cells relative to the total nuclei count was used as an index of effector caspase activation.

Image Analysis

In vitro experiments: Quantitative image analysis —including propidium iodide staining, caspase-3/7 activity, and basal fluorescence measurements of XIAP and miR-199a-5p— was performed using the QuPath software v0.4.3. The cell detection module was used to identify all nuclei based on DAPI fluorescence. For each detected cell, a 5 μm ellipsoidal region of interest (ROI) was automatically positioned over the cytoplasm to measure the mean fluorescence intensity in the corresponding channel. For XIAP immunofluorescence, signal intensity was quantified in the Alexa 488 channel (λ_ex/em ≈ 495/519 nm). For caspase-3/7 activity, fluorescence was measured in the same spectral range corresponding to the CellEvent™ Caspase-3/7 Green Detection Reagent (λ_ex/em ≈ 502/530 nm), compatible with FITC/GFP filter sets. For propidium iodide (PI) staining, intensity was analyzed in the red channel (λ_ex/em ≈ 535/617 nm). A total of 556 cells (A2780) and 564 cells (A2780cis) were analyzed for the basal quantification of XIAP and miR-199a-5p fluorescence (n=3 independent experiments). For PI and caspase-3/7 activity assays, approximately 1,500 cells per condition were analyzed across five non-overlapping fields per replicate from n=4 independent experiments. Mean fluorescence intensity values were exported from QuPath for subsequent statistical analysis.

Human tissues: FISH/IF images from stained human ovarian tissue sections were acquired on a fully motorized Olympus IX83 microscope (Olympus, Tokyo, Japan) using CellSens Dimensions software v4.1.1 (Olympus). Image analysis was performed in QuPath v0.4.3 using a custom macro developed in-house. Briefly, ten regions of interest (ROIs; 750 × 750 μm each) were defined per sample to cover the largest possible fraction of the section and thereby obtain an unbiased representation of the tissue. Nuclei were then automatically detected within each ROI using the DAPI channel, yielding ~35,500–36,000

nuclei per ROI. To approximate whole-cell signal, nuclear detections were isotropically expanded by 3 μm to generate cell masks. Mean pixel intensities were then quantified for each detected cell in the FITC channel (XIAP, green) and the Cy5 channel (miR-199a-5p, red), and measurements were exported as ROI-level CSV files for downstream analysis.

Following QuPath export, colocalization metrics between XIAP (FITC) and miR-199a-5p (Cy5) were computed in a blinded manner using R (≥4.2) within the tidyverse framework (dplyr and purrr), together with base R functions for file handling and summary statistics. All ROI-level CSV files exported from QuPath (filtered colocalization outputs; file name pattern: coloc_filtrado.csv) were automatically identified and processed using a standardized pipeline. For each file, the script verified the presence of the expected columns (ROI identifier and per-cell mean pixel intensities for FITC and Cy5). Channel-specific intensity thresholds were then defined using the 25th percentile of the per-cell mean pixel intensity distribution (FITC_mean and Cy5_mean, respectively). Colocalization was quantified per ROI by computing (i) the Pearson correlation coefficient between FITC_mean and Cy5_mean across all detected cells within the ROI (set to missing when either channel showed zero variance), and (ii) Manders' overlap coefficients, defined as M1 = Σ(Cy5_mean in cells with FITC_mean > threshold_FITC)/Σ(Cy5_mean) and M2 = Σ(FITC_mean in cells with Cy5_mean > threshold_Cy5)/Σ(FITC_mean). In addition, ROI-level cross-correlation descriptors exported by QuPath (CCF_MAX, CCF_MIN, K1, K2, and FWHM) were extracted directly from their corresponding columns and summarized alongside Pearson and Manders' coefficients. ROI-level outputs were compiled into a single table and subsequently averaged across the ten ROIs per image to generate one mean value per image for each metric. To preserve blinding during downstream analyses, group labels were intentionally left blank at the image-summary stage. Both ROI-level and image-level outputs were exported as CSV files for statistical analysis. Accordingly, for each image, a single representative value per metric was obtained by averaging the ROI-level measurements across the ten ROIs.

Statistical Analysis

Statistical analyses were selected according to experimental design and data structure, and were conducted using GraphPad Prism and R software. Linear mixed-effects models (LMMs) were used as the primary framework for most functional assays, including cell viability (MTT), membrane integrity (propidium iodide, PI), caspase-3/7 activation (fluorometric readouts and Western blot–based endpoints), and XIAP protein levels under treatment. In LMMs, transfection status (miR-199a-5p) and cisplatin treatment, as well as their interaction, were modeled as fixed effects, while experimental day was included as a random intercept to account for inter-experimental variability. Fixed-effect coefficients were tested using t-statistics with Satterthwaite's approximation for denominator degrees of freedom, as implemented in the "lmerTest" package. When appropriate, post hoc pairwise contrasts were adjusted using Tukey's method after LMM fitting in multi-group settings (MTT, PI, and caspase assays) to control type I error. For simple two-group comparisons under basal conditions, parametric Student's t-tests were applied to RT–qPCR measurements (basal miR-199a-5p and XIAP expression in A2780 versus A2780cis), whereas basal FISH/IF fluorescence intensities were compared using

Mann–Whitney U tests. A paired one-tailed t-test was used for densitometric quantification of basal XIAP Western blots following miR-199a-5p transfection in matched experiments, justified by an a priori directional hypothesis of XIAP reduction. For analyses in human tissue and single-cell intensity distributions that violated normality and/or homoscedasticity assumptions, non-parametric and variance-robust tests were employed: Mann–Whitney U tests were used for M1, K1 and FWHM, whereas Welch's t-tests were applied to Pearson, M2, CCF_MAX, CCF_MIN and K2. In silico prediction of miR-199a-5p binding to XIAP mRNA was performed using STarMir, which applies logistic regression to estimate site functionality (LogitProb) from CLIP-trained models.

Multivariate structure within the nine-parameter colocalization dataset was further interrogated by principal component analysis (PCA). Statistical tests were two-sided unless otherwise stated, and significance was defined as $p < 0.05$.

RESULTS

XIAP is a direct downstream target of miR-199a-5p

In our previous study[13], we identified seven microRNAs that target the 3'-UTR of rat XIAP mRNA using in silico techniques: miR-181a, miR-181b, miR-181c-5p, miR-199a-5p, miR-21-5p, and miR-340-5p. Particularly, we used PITA software to examine the target site accessibility of miR-199a-5p on the mRNA secondary structure16. We observed a canonical seed pairing and favorable hybridization energies in both human and mouse XIAP 3′ untranslated region (3′UTR) (ΔG_hybrid = −15.4 and −15.2 kcal/mol, respectively; Figure 1A).
We employed the STarMir tool, which incorporates humans and mice CLIP-based interaction data[17,18], to verify target site accessibility in a biological context. The results confirmed the accessibility and binding probability of miR-199a-5p to both human and mouse XIAP 3′UTRs. Logistic probabilities (LogitProb) for binding were 0.543 in human and 0.594 in mouse, both exceeding the 0.5 threshold indicative of favorable interaction (Figure 1B). These results support a thermodynamically stable and evolutionarily conserved interaction between miR-199a-5p and XIAP across species.

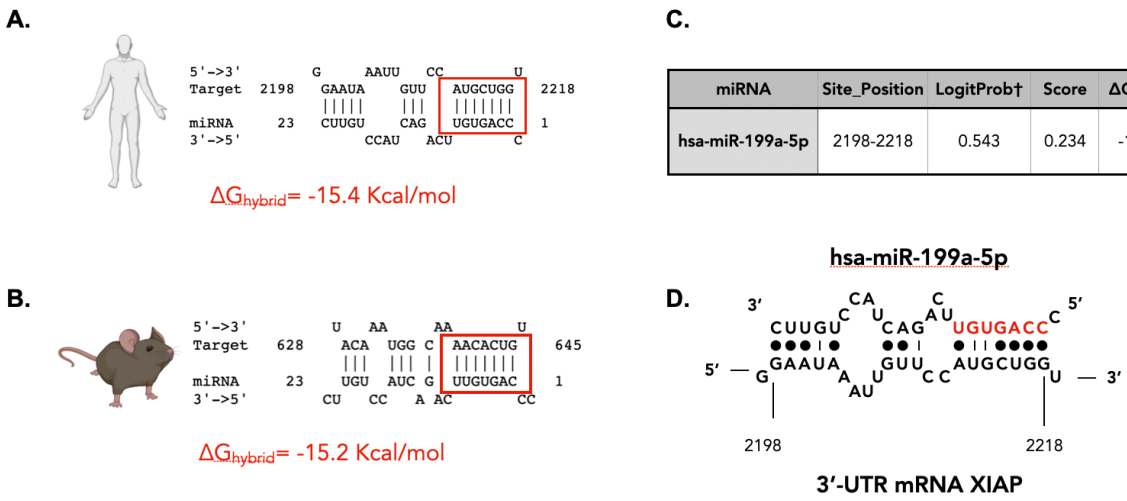

Figure 1. Computational prediction of miR-199a-5p binding sites within the 3'UTR of XIAP mRNA in human and mouse. (A) Predicted duplex formation between hsa-miR-199a-5p and the 3' untranslated region (3'UTR) of human XIAP mRNA (positions 2198–2218), showing canonical seed pairing and extended base complementarity. (B) Conserved interaction between miR-199a-5p and the murine ortholog of XIAP (positions 628–645), also exhibiting canonical seed pairing and a comparable ΔG_hybrid of −15.2 kcal/mol. (C) Summary table of STarMir predictions for the human target site. The Site_Position refers to the nucleotide coordinates of the predicted target region within the human XIAP 3'UTR (based on RefSeq). LogitProb† indicates the probability of the site being a true miRNA binding site, calculated using a logistic regression model trained on crosslinking-immunoprecipitation (CLIP) datasets; values >0.5 are considered supportive of functional binding. The Score reflects a composite measure incorporating multiple binding determinants, including seed pairing strength, 3' pairing, target site accessibility, AU-rich flanking context, and hybridization energy. A higher score suggests stronger predicted binding affinity. ΔG_hybrid represents the Gibbs free energy (kcal/mol) of miRNA:mRNA duplex formation; more negative values denote greater thermodynamic stability. (D) RNA secondary structure model of the XIAP 3'UTR surrounding the predicted binding site for miR-199a-5p, generated using RNAfold. The seed region of the miRNA is highlighted in red. Black dots indicate base pairing between the miRNA and the target mRNA.

Characterization of the miR-199/XIAP Regulatory Axis in Cisplatin-Sensitive and Cisplatin-Resistant Ovarian Cancer Cells

The inhibitor of apoptosis protein XIAP is a key modulator of cell survival pathways and has been implicated in the development of chemoresistance in ovarian cancer19. Similarly, miR-199a-5p has been identified as a relevant regulator of drug response in this type of cancer20–22. To study the role of the miR-199/XIAP regulatory axis in cisplatin resistance, we analyzed its expression and functional relationship in cisplatin-sensitive (A2780) and cisplatin-resistant (A2780cis) ovarian cancer cell lines.

Differential Expression of miR-199a-5p and XIAP in Cisplatin-Resistant Cells

We next assessed the expression levels of miR-199a-5p and XIAP in both cell lines. TaqMan-based RT-qPCR analysis revealed a significant downregulation of miR-199a-5p in A2780cis cells relative to A2780, with a fold change of –2.58 (t_4=3.46, p=0.013; n=3; Figure 2A, above). In contrast, XIAP transcript levels were not significantly altered between the two lines (t_4=1.106, p=0.165; n=3; Figure 2A, below).

XIAP Protein Expression in Ovarian Cancer Cell Lines

Western blot analysis was performed on whole-cell lysates obtained from three independent matched experiments to compare XIAP protein abundance between A2780 and A2780cis cells (Figure 2B). Densitometric quantification of XIAP, normalized to β-actin, showed slightly higher mean expression in A2780cis cells (1.52 ± 0.41) relative to A2780 cells (1.27 ± 0.31). However, this difference did not reach statistical significance (t_2=1.709, p=0.11; one-tailed paired t-test; 95% CI: –0.861 to 0.3), indicating that XIAP protein levels were comparable between the two cell lines under basal conditions.

Single-Cell Validation of miR-199a-5p and XIAP Expression by FISH and Immunofluorescence

To further validate and localize these expression patterns at the single-cell level, we conducted combined FISH (miR-199a-5p) and immunofluorescence (XIAP) staining across three independent experiments (Figure XC). Quantitative image analysis showed single-cell intensity distributions that were consistent with the trends observed by qPCR and Western blot. XIAP fluorescence intensity was moderately elevated in A2780cis (102.8 ± 44.0) compared to A2780 (91.2 ± 27.3), although this difference did not reach statistical significance ($p = 0.209$; Mann–Whitney U test). In contrast, miR-199a-5p levels were lower in A2780cis (41.2 ± 21.7 a.u.) relative to A2780 (60.5 ± 27.9 a.u.; $p = 0.009$), supporting downregulation in the resistant phenotype (Figure 2C).

A.

	ΔCt	T-test			fold decrease	
		mean diff (ΔΔCt)		p value		
A2780	3.89 ± 0.41	**A2780 vs. A2780 cis**	1.37 (0.27, 2.41)	$T_4 = 3.46$	0.387	(0.188 , 0.829)
A2780 cis	6.44 ± 2.11			**p = 0.013 (*)**		

	ΔCt	T-test			fold increase	
		mean diff (ΔΔCt)		p value		
A2780	13.001 ± 0.63	**A2780 vs. A2780 cis**	-0.472 (-1.656 , 0.712)	$T_4 = 1.106$	1.387	(0.61 , 3.151)
A2780 cis	12.53 ± 0.232			p = 0.165		

B.

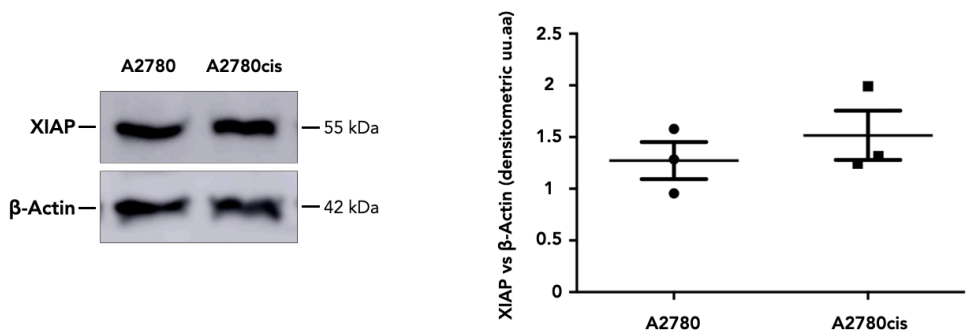

C.

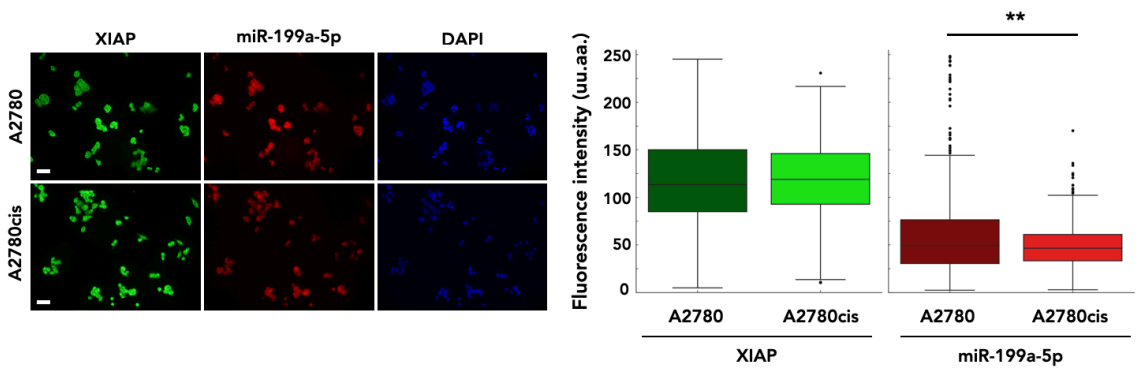

Figure 2. Basal expression of miR-199a-5p and XIAP in cisplatin-sensitive (A2780) and -resistant (A2780cis) ovarian cancer cell lines. (A) Statistical analysis of RT-qPCR results is shown in the accompanying table, using a Student's t-test ($p < 0.05$). (B) Representative immunoblot showing basal

expression of XIAP and β-actin in A2780 and A2780cis cells (left). Dot plot summarizing densitometric quantification of XIAP protein levels normalized to β-actin (right). Data represent mean ± SEM from n=3 independent experiments. (C) Immunofluorescence analysis of A2780 (upper panel) and A2780cis (lower panel) cells showing basal expression of XIAP (green) and miR-199a-5p (red), with nuclei counterstained using DAPI (blue). Scale bar = 50 µm. Boxplots on the right show fluorescence intensity quantification for each marker. Statistical analysis was performed using Mann–Whitney U tests).

Differential regulation of XIAP by miR-199a-5p in ovarian cancer cells under basal conditions

To examine the effect of miR-199a-5p on XIAP expression under untreated conditions, paired analyses were conducted in cisplatin-sensitive (A2780) and cisplatin-resistant (A2780cis) ovarian cancer cell lines (Figure 3A). In A2780 cells, transfection with miR-199a-5p significantly reduced XIAP protein levels compared with negative control (one-tailed paired t-test, p=0.0359, n=6) (Figure 3B, left). This decrease indicates a downregulation of XIAP under untreated conditions in this cisplatin-sensitive line. In contrast, miR-199a-5p transfection produced a no statistically significant change in XIAP expression was detected in the cisplatin-resistant A2780cis cells (p = 0.0765, n=5) (Figure 3B, right).

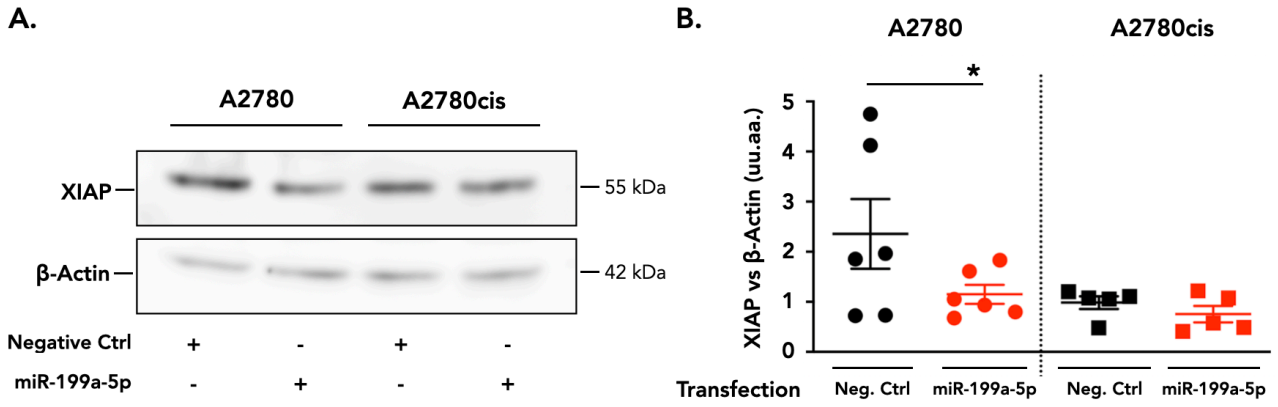

Figure 3. Effect of miR-199a-5p transfection on XIAP protein expression in A2780 and A2780cis ovarian cancer cells under basal conditions. (A) Representative Western blot of XIAP in whole-cell lysates from A2780 (left) and A2780cis (right) ovarian cancer cells transfected with either a negative control mimic (Neg.Ctrl) or miR-199a-5p mimic under basal conditions. β-Actin was used as a loading control. (B) Densitometric analysis of XIAP normalized to β-actin from six independent experiments in A2780 cells (circles) and five in A2780cis cells (squares). Statistical evaluation was performed using one-tailed paired t-tests. Asterisks indicate statistically significant differences ($p < 0.05$).

miR-199a-5p Enhances Cisplatin-Induced Cytotoxicity in Ovarian Cancer Cells via Increased Cell Death

To investigate whether miR-199a-5p modulates cisplatin-induced cytotoxicity in ovarian cancer cells, we assessed the study of membrane integrity (Propidium iodide (PI) staining), apoptotic activity (caspase-3/7 fluorescence and immunoblot), and levels of the apoptosis inhibitor XIAP in both cisplatin-sensitive (A2780) and cisplatin-resistant (A2780cis) cancer cell lines.

Validation of the Cisplatin-Resistant Phenotype

To confirm the resistant phenotype of the A2780cis cell line, we performed MTT assays comparing its response to cisplatin treatment with that of parental A2780 cells. As expected, A2780cis cells exhibited a higher survival rate upon cisplatin exposure than parental A2780 cells. This was reflected by a higher EC_{50} in A2780cis cells (44.56 μM) compared with A2780 cells (12.16 μM) (Figure 4), confirming the chemoresistant phenotype of the A2780cis cell line.

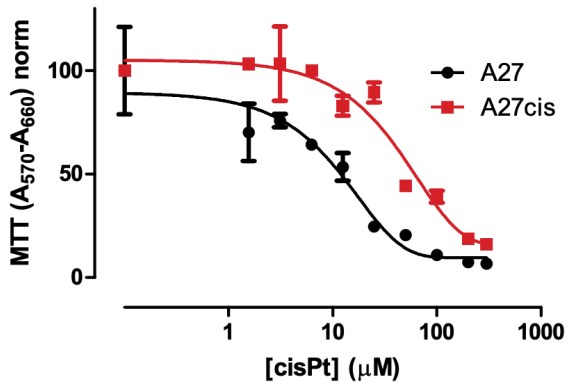

Figure 4. Cisplatin sensitivity of A2780 and A2780cis ovarian cancer cell lines. Dose–response curves were generated from MTT assays after 72-hour treatment with increasing concentrations of cisplatin. EC_{50} values were calculated to compare drug sensitivity between the cell lines. Data represent the mean ± SEM from three independent experiments performed in triplicate.

Distinct effects of miR-199a-5p on cisplatin response in sensitive and resistant ovarian cancer cells

To evaluate the impact of miR-199a-5p on cisplatin sensitivity, cell viability was assessed in A2780 and A2780cis ovarian cancer cells using the MTT assay following transfection with either miR-199a-5p or a negative control, in the presence or absence of cisplatin (Figure 5)

In A2780 cells (Figure 5, left), the linear mixed-effects model without interaction revealed significant main effects of cisplatin treatment ($F(1,7) = 15.30$, $p = 0.0058$) and miR-199 transfection ($F(1,7) = 10.66$, $p = 0.0138$) on cell viability. Cisplatin alone reduced viability by 17.5% compared to untreated controls (0.4117 ± 0.0514 vs. 0.4988 ± 0.0514; $p = 0.0234$), while miR-199 alone reduced viability by 14.6%, though this was not statistically significant (0.4261 ± 0.0514 vs. 0.4988 ± 0.0514; $p = 0.0531$). In miR-199–transfected cells, cisplatin further reduced viability by 20.5% (0.3390 ± 0.0514 vs. 0.4261 ± 0.0514; $p = 0.0234$). In cisplatin-treated cells, miR-199 transfection tended to reduce viability by 17.8%, although this difference did not reach statistical significance (0.3390 ± 0.0514 vs. 0.4117 ± 0.0514; $p = 0.0531$). The combined treatment (miR-199 + cisplatin) reduced viability by 32.1% relative to untreated controls (0.3390 ± 0.0514 vs. 0.4988 ± 0.0514; $p = 0.0061$). This reduction was numerically consistent with the sum of the individual effects of cisplatin (−0.0871) and miR-199 (−0.0727), supporting an additive interpretation.

In contrast, neither miR-199a-5p transfection nor cisplatin treatment significantly altered viability in A2780cis cells (Figure 5, right). The model detected no main effect of

miR-199a-5p (F(1,7) = 0.44, p = 0.530) or cisplatin (F(1,7) = 3.40, p = 0.108), and their combination did not reduce viability (0.316 ± 0.021 vs. 0.298 ± 0.021; Tukey p = 0.7343).

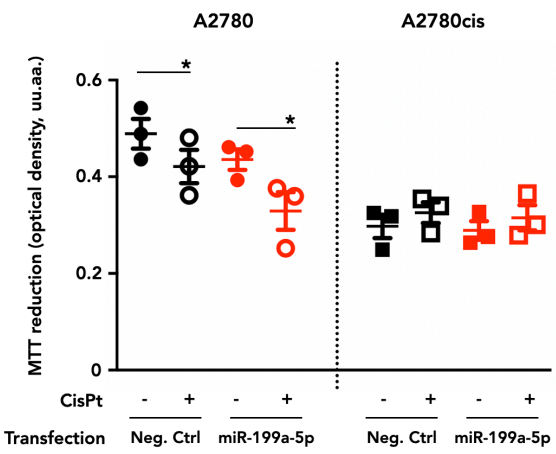

Figure 5. Effect of miR-199a-5p and cisplatin on cell viability in A2780 and A2780cis cells. A2780 (circles) and A2780cis (squares) ovarian cancer cells were transfected with either a negative control mimic (NC) or a miR-199a-5p mimic, and subsequently treated with or without 12.5 μM cisplatin (cisPt) for 24 h. Cell viability was determined by MTT assay and expressed as optical density (OD_{570}–OD_{660}). Each point corresponds to an individual replicate, n=3; bars indicate mean ± S.E.M. Circles represent A2780 cells: filled symbols correspond to untreated conditions (cisPt–) and open symbols to cisplatin treatment (cisPt+). Squares represent A2780cis cells, following the same visual code. Color indicates transfection condition: black for negative control, and red for miR-199a-5p-transfected cells. Pairwise comparisons were conducted using Tukey-adjusted post hoc tests p-values: $p < 0.05$ (*).

Propidium iodide staining reveals enhanced cell death with combined treatment

PI staining assays were performed on A2780 (Figure 6A) and A2780cis cells (Figure 6B) transfected with either a miR-199a-5p mimic or a negative control, followed by 12.5 μM cisplatin treatment for 24 hours.

In A2780 cells, the linear mixed-effects model identified statistically significant effects of miR-199a-5p (F(1,9)=7.6558, p=0.02186) and the miR-199a-5p × cisplatin interaction (F(1,9)=6.7081, p=0.02921), whereas the main effect of cisplatin was not significant (F(1,9)=2.5721, p=0.14323), indicating that PI positivity depended on transfection status and its interplay with cisplatin treatment (Figure 6C, left). Tukey-adjusted post-hoc comparisons confirmed that the combined treatment significantly increased PI-positive cells relative to cisplatin alone (t(9)=−3.788, p=0.0185) (Figure 6C, left). Additionally, non-significant trends were observed for the comparisons with untreated controls (t(9)=−3.091, p=0.0524) and miR-199a-5p alone (t(9)=−2.965, p=0.0633). No significant differences were detected between untreated controls and either single treatment (miR-199a-5p: t(9)=−0.125, p=0.9992; cisplatin: t(9)=0.697, p=0.8956), or between the two single treatments (t(9)=0.822, p=0.8426).

In the cisplatin-resistant A2780cis line (Figure 6C, right), the linear mixed-effects model did not identify statistically significant main effects of miR-199a-5p (F(1,9)=0.1223, p=0.73460) or cisplatin (F(1,9)=4.0582, p=0.07478), nor a significant interaction between the two treatments (F(1,9)=3.0564, p=0.11436).

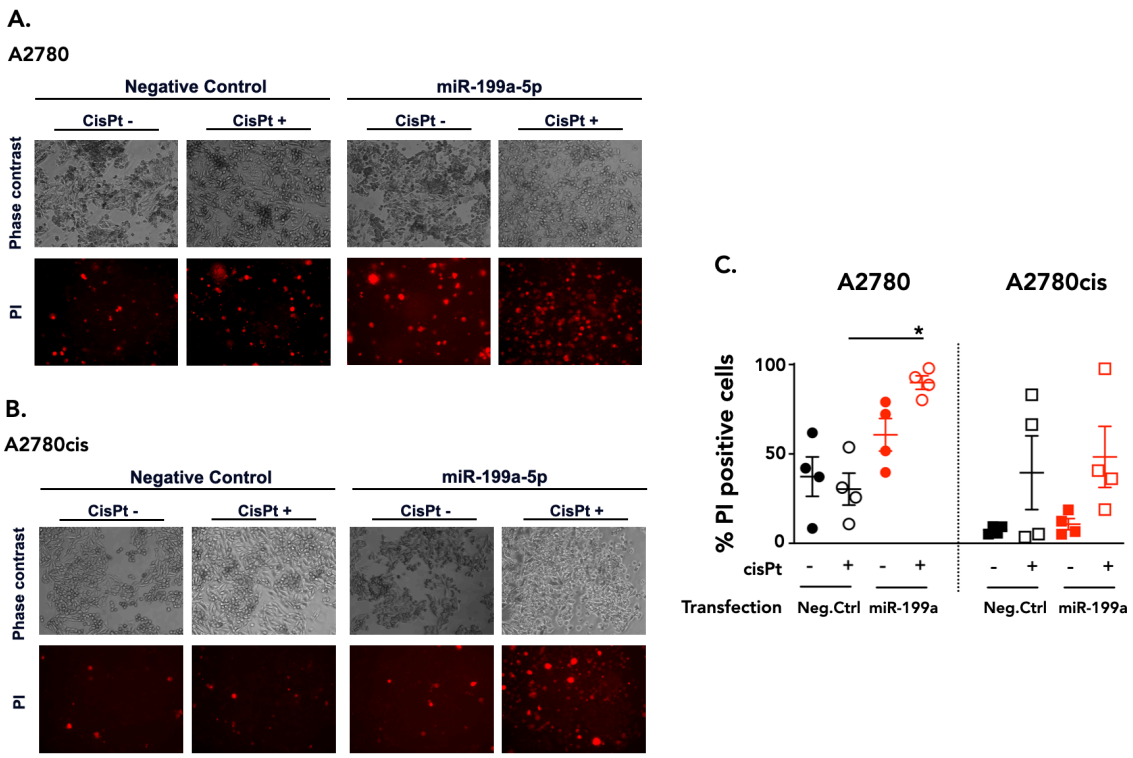

Figure 6. miR-199a-5p enhances cisplatin-induced cell death in ovarian cancer cells. (A–B) Representative epifluorescence images showing phase contrast and propidium iodide (PI)-positive cells (red) in A2780 (A) and A2780cis (B) cells transfected with a negative control mimic (Neg. Ctrl) or miR-199a-5p mimic and treated or not with 12.5 μM cisplatin (CisPt) for 24 hours. (C) Quantification of PI-positive cells (%), expressed as mean ± SD from four independent experiments. Statistical analysis was performed using a linear mixed-effects model including the interaction between miR-199a-5p transfection and cisplatin treatment as fixed effects, and experimental day as a random intercept. Pairwise comparisons were conducted using Tukey-adjusted post hoc tests. *$p < 0.05$.

miR-199a-5p Increases Propaptotic Activation in Response to Cisplatin in Ovarian Cancer Cells

To assess the pro-apoptotic effects of miR-199a-5p in the context of cisplatin treatment, we quantified caspase-3/7-positive cells by fluorescence microscopy in both A2780 and A2780cis ovarian cancer cell lines. This assay measures effector caspases-3/7 enzymatic activity, indicators of early-stage apoptotic signaling.

Caspase-3/7 activity was quantified in A2780 and A2780cis cells transfected with miR-199a-5p or a negative control and treated with or without 12.5 μM cisplatin for 24 h.

In the cisplatin-sensitive A2780 line, cisplatin significantly increased the proportion of caspase-positive cells ($F(1,12)=27.8896$, $p=0.0001943$), whereas neither miR-199a-5p transfection ($F(1,12)=3.2912$, $p=0.0947176$) nor the interaction between factors ($F(1,12)=0.6172$, $p=0.4473206$) reached statistical significance (Figure 7A, upper panel; Figure 7B, left graph). Post hoc tests comparisons showed that cisplatin significantly increased caspase-3/7 activity relative to untreated controls both in negative control–transfected cells ($t(9)=-3.179$, $p=0.0459$) and in miR-199a-5p–transfected cells ($t(9)=-4.290$, $p=0.0090$), while no differences were detected between transfection

conditions either in the absence of cisplatin (t(9)=−0.727, p=0.8838) or under cisplatin treatment (t(9)=−1.838, p=0.3174).

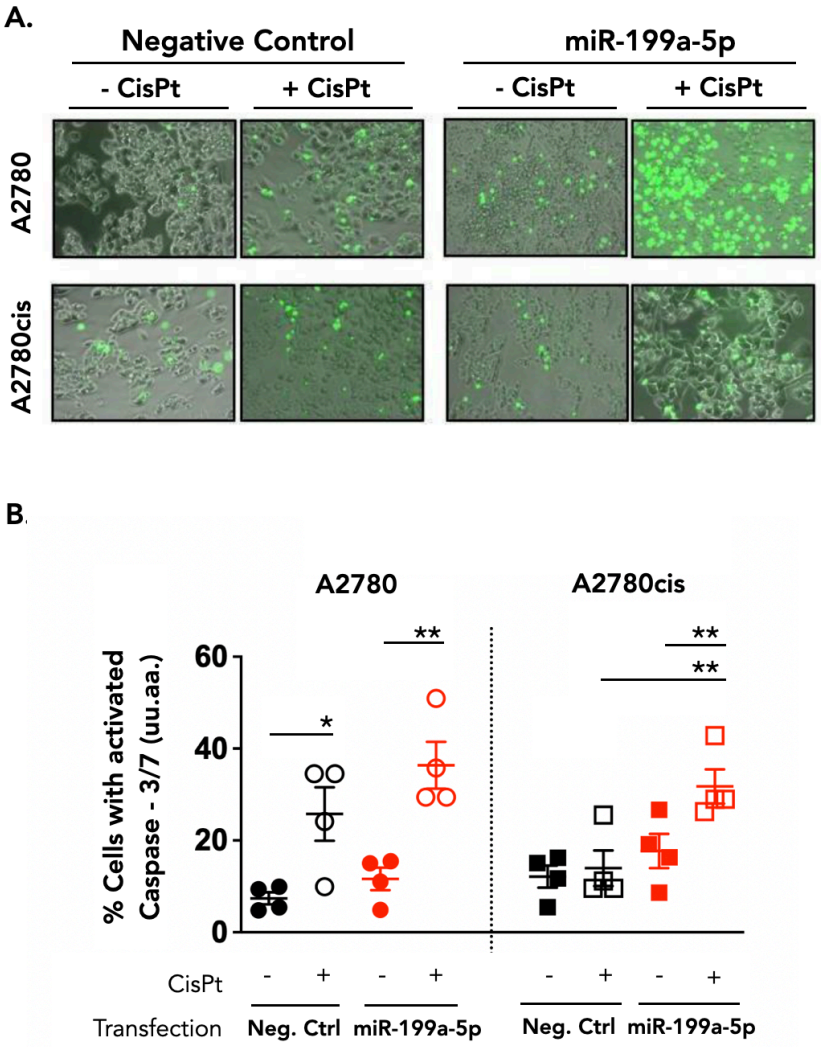

Figure 7. miR-199a-5p enhances cisplatin-induced caspase-3/7 activation in ovarian cancer cells. A. Representative fluorescence microscopy images showing caspase-3/7–positive cells (green) in A2780 and A2780cis ovarian cancer cell lines transfected with either a negative control mimic or miR-199a-5p mimic, and treated or not with 12.5 μM cisplatin (CisPt) for 24 hours. (B) Quantification of the percentage of caspase-3/7–positive cells is shown for A2780 (left, circles) and A2780cis (right, squares). Each dot represents one independent experiment (n = 4). Statistical significance was assessed using linear mixed-effects models with experimental day as a random effect, followed by Tukey-adjusted post hoc tests for pairwise comparisons. Asterisks indicate statistically significant differences between groups: p<0.05 (*), p<0.01 (**).

In A2780cis cells, cisplatin (F(1,9)=11.4521, p=0.008074), miR-199a-5p transfection (F(1,9)=25.5065, p=0.000690), and their interaction (F(1,9)=6.9905, p=0.026740) all produced significant effects, indicating that caspase-3/7 activation depended on the combination of both treatments (Figure 7A, lower panel; Figure 7B, right graph). Tukey-corrected post-hoc comparisons showed that, under cisplatin exposure, miR-199a-5p transfection significantly increased caspase-3/7 activity relative to negative control–

transfected cells ($t(9)=-5.441$, $p=0.0019$), and that cisplatin significantly increased caspase-3/7 activity in miR-199a-5p–transfected cells ($t(9)=-4.262$, $p=0.0093$), whereas no transfection difference was observed in the absence of cisplatin ($t(9)=-1.702$, $p=0.3766$) and cisplatin alone did not differ from untreated controls in negative control–transfected cells ($t(9)=-0.523$, $p=0.9513$).

Caspase-3 activation in response to miR-199a-5p and cisplatin in ovarian cancer cells

To assess whether miR-199a-5p modulates XIAP protein levels in the context of cisplatin exposure, XIAP expression was quantified by Western blot in whole-cell lysates from A2780 and A2780cis ovarian cancer cells, followed by densitometric analysis normalized to loading controls.

In A2780 cells, the linear mixed-effects model identified a significant main effect of cisplatin on XIAP levels ($F(1,9)=9.3062$, $p=0.01378$), whereas the main effect of miR-199a-5p transfection was not significant ($F(1,9)=1.9051$, $p=0.20082$) and the interaction term showed a non-significant trend ($F(1,9)=3.9819$, $p=0.07711$). Tukey-adjusted post-hoc comparisons indicated that cisplatin significantly reduced XIAP relative to untreated controls in negative control–transfected cells ($t(9)=3.568$, $p=0.0256$), and that XIAP levels in the combined miR-199a-5p + cisplatin condition also differed from untreated negative controls ($t(9)=3.133$, $p=0.0492$), while no differences were detected between transfection conditions either in the absence of cisplatin ($t(9)=2.387$, $p=0.1492$) or under cisplatin exposure ($t(9)=-0.435$, $p=0.9709$).

In A2780cis cells, the linear mixed-effects model identified a significant interaction between miR-199a-5p transfection and cisplatin treatment ($F(1,9)=12.9292$, $p=0.005787$), whereas the main effects of transfection ($F(1,9)=2.7892$, $p=0.129243$) and cisplatin ($F(1,9)=0.8596$, $p=0.378037$) were not significant. Post-hoc comparisons showed that cisplatin significantly reduced XIAP relative to untreated controls in negative control–transfected cells ($t(9)=3.198$, $p=0.0446$), whereas the combined miR-199a-5p + cisplatin condition did not differ from untreated negative controls ($t(9)=-0.525$, $p=0.9508$); within cisplatin-treated cells, XIAP levels differed significantly between transfection conditions (negative control + cisplatin vs miR-199a-5p + cisplatin: $t(9)=-3.723$, $p=0.0203$), while no transfection difference was detected in the absence of cisplatin ($t(9)=1.362$, $p=0.5507$).

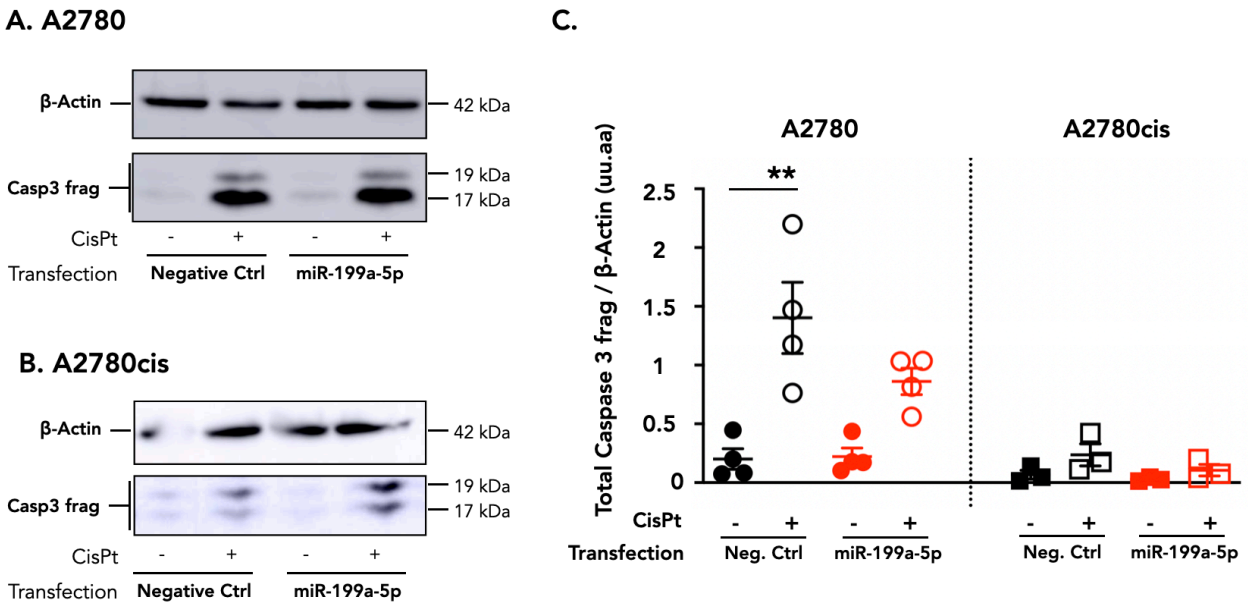

Figure 8. Effects of cisplatin and miR-199a-5p on cleaved caspase-3 levels in ovarian cancer cells. (A–B) Western blot analysis of cleaved caspase-3 (Casp3 frag) in whole-cell lysates of A2780 (A, upper panel) and A2780cis (B, lower panel) ovarian cancer cells transfected with either a negative control mimic (NegCtrl) or miR-199a-5p mimic, and treated or not with cisplatin (CisPt, 12.5 μM, 24 h). β-Actin was used as a loading control. (C) Densitometric quantification of cleaved caspase-3 bands normalized to β-actin from four independent experiments in A2780 (left, circles) and three in A2780cis (right, squares) cells. Tukey-adjusted post hoc tests. **$p < 0.01$).

Differential regulation of XIAP by miR-199a-5p and cisplatin

To evaluate the regulation of XIAP by miR-199a-5p under cisplatin exposure, Western blot analyses were performed in A2780 (Figure 9A, left panel) and A2780cis cells (Figure 9A, right panel) transfected with a miR-199a-5p mimic or a negative control and treated or not with 12.5 μM cisplatin (Figure 9). XIAP protein abundance was quantified by densitometry and normalized to β-actin.

In A2780 ovarian cancer cells, the linear mixed-effects model identified a significant main effect of cisplatin on XIAP levels ($F(1,9)=9.3062$, $p=0.01378$), whereas the main effect of miR-199a-5p did not reach statistical significance ($F(1,9)=1.9051$, $p=0.20082$) and the interaction term showed a non-significant trend ($F(1,9)=3.9819$, $p=0.07711$). Consistent with basal repression, the model-based test for the miR-199a-5p coefficient at the reference cisplatin level (untreated) was significant ($t(9)=-2.387$, $p=0.040756$), in line with reduced XIAP following miR-199a-5p transfection under untreated conditions (Figure 3A,B; $p=0.0359$, $n=6$). Tukey-adjusted post-hoc comparisons indicated that cisplatin significantly reduced XIAP relative to untreated controls in negative control–transfected cells ($t(9)=3.568$, $p=0.02569$), whereas cisplatin did not significantly alter XIAP in miR-199a-5p–transfected cells ($t(9)=0.746$, $p=0.8761$) (Figure 9B, left graph). Moreover, no differences were detected between transfection conditions either in the absence of cisplatin ($t(9)=2.387$, $p=0.1492$) or under cisplatin exposure ($t(9)=-0.435$, $p=0.9709$).

In contrast, in A2780cis ovarian cancer cells (Figure 9B, right graph), the linear mixed-effects model identified a significant interaction between miR-199a-5p transfection and

cisplatin treatment (F(1,9)=12.9292, p=0.005787), whereas the main effects of miR-199a-5p (F(1,9)=2.7892, p=0.129243) and cisplatin (F(1,9)=0.8596, p=0.378037) were not significant. Tukey-adjusted post-hoc comparisons showed that cisplatin significantly reduced XIAP relative to untreated controls in negative control–transfected cells (t(9)=3.198, p=0.0446), whereas the combined miR-199a-5p + cisplatin condition did not differ from untreated negative controls (t(9)=−0.525, p=0.9508). Within cisplatin-treated cells, XIAP levels were significantly higher in miR-199a-5p–transfected cells than in negative control–transfected cells (negative control + cisplatin vs miR-199a-5p + cisplatin: t(9)=−3.723, p=0.0203), while no transfection difference was detected in the absence of cisplatin (t(9)=1.362, p=0.5507).

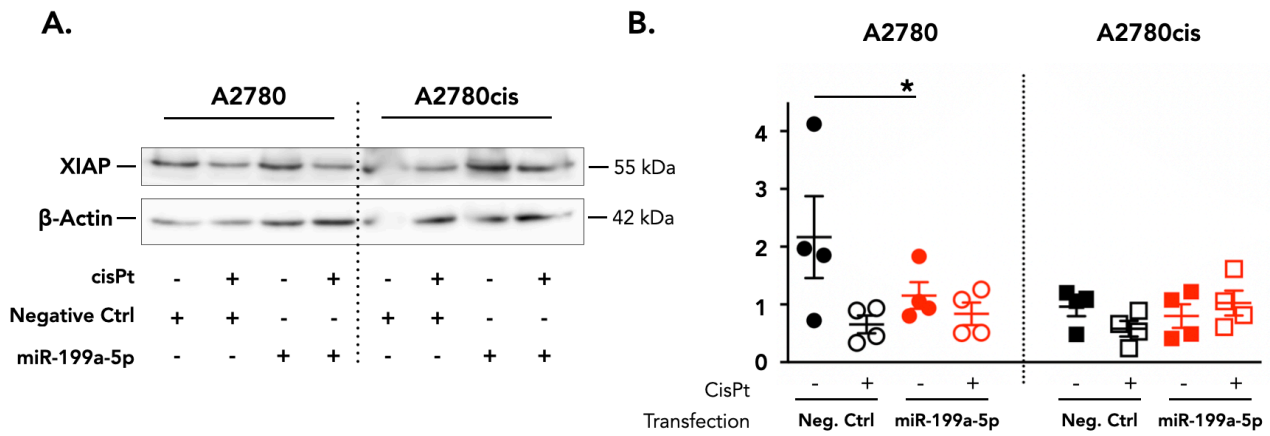

Figure 9. Effects of cisplatin and miR-199a-5p on XIAP protein levels in ovarian cancer cells. (A) Representative Western blot analysis of XIAP in whole-cell lysates from A2780 (left side) and A2780cis (right side) ovarian cancer cells transfected with either a negative control mimic (Neg. Ctrl) or miR-199a-5p mimic and treated or not with cisplatin (CisPt, 12.5 μM, 24 h). β-Actin was used as a loading control. (B) Densitometric quantification of XIAP bands normalized to β-actin from four independent experiments in A2780 (left, circles) and A2780cis (right, squares). Tukey-adjusted post hoc tests. *p < 0.05.

Spatial and Subcellular Co-localization of miR-199a-5p and XIAP in human ovarian tissue and in HGSOC.

To characterize the spatial and subcellular distribution of miR-199a-5p and its predicted target XIAP in human ovarian tissue, multiplex fluorescence in situ hybridization (FISH) combined with immunofluorescence (IF) was performed on FFPE sections from non-neoplastic ovaries and high-grade serous ovarian carcinoma (HGSOC) samples. At low magnification (10x; Figure 10A), healthy ovarian tissue displayed intense XIAP staining predominantly localized within glandular epithelial structures, whereas miR-199a-5p signal was weak and largely confined to stromal regions. In contrast, HGSOC samples exhibited strong and widespread miR-199a-5p expression across both epithelial and stromal compartments, while XIAP remained detectable but with a more heterogeneous distribution (Figure 10B).

At intermediate magnification (Figure 10C), XIAP localization in control tissue remained restricted to epithelial territories, with minimal overlap with miR-199a-5p, which was largely excluded from these regions (Figure 10C, upper panel). In tumor tissue, however, both signals were detected within overlapping cellular domains, producing merged

fluorescence indicative of partial spatial colocalization (10C, lower panel). At high-resolution, imaging further showed that in normal ovary, XIAP was cytoplasmically localized in epithelial cells, whereas miR-199a-5p remained faint and peripherally distributed (Figure 10D, left). In HGSOC cells, miR-199a-5p exhibited strong cytoplasmic and prominent perinuclear—and occasionally nuclear—localization, a pattern absent in control tissue (Figure 10D, right). This intranuclear signal was confirmed at higher magnification, where miR-199a-5p overlapped with DAPI-stained nuclei in numerous tumor cells (Figure 10E, right).

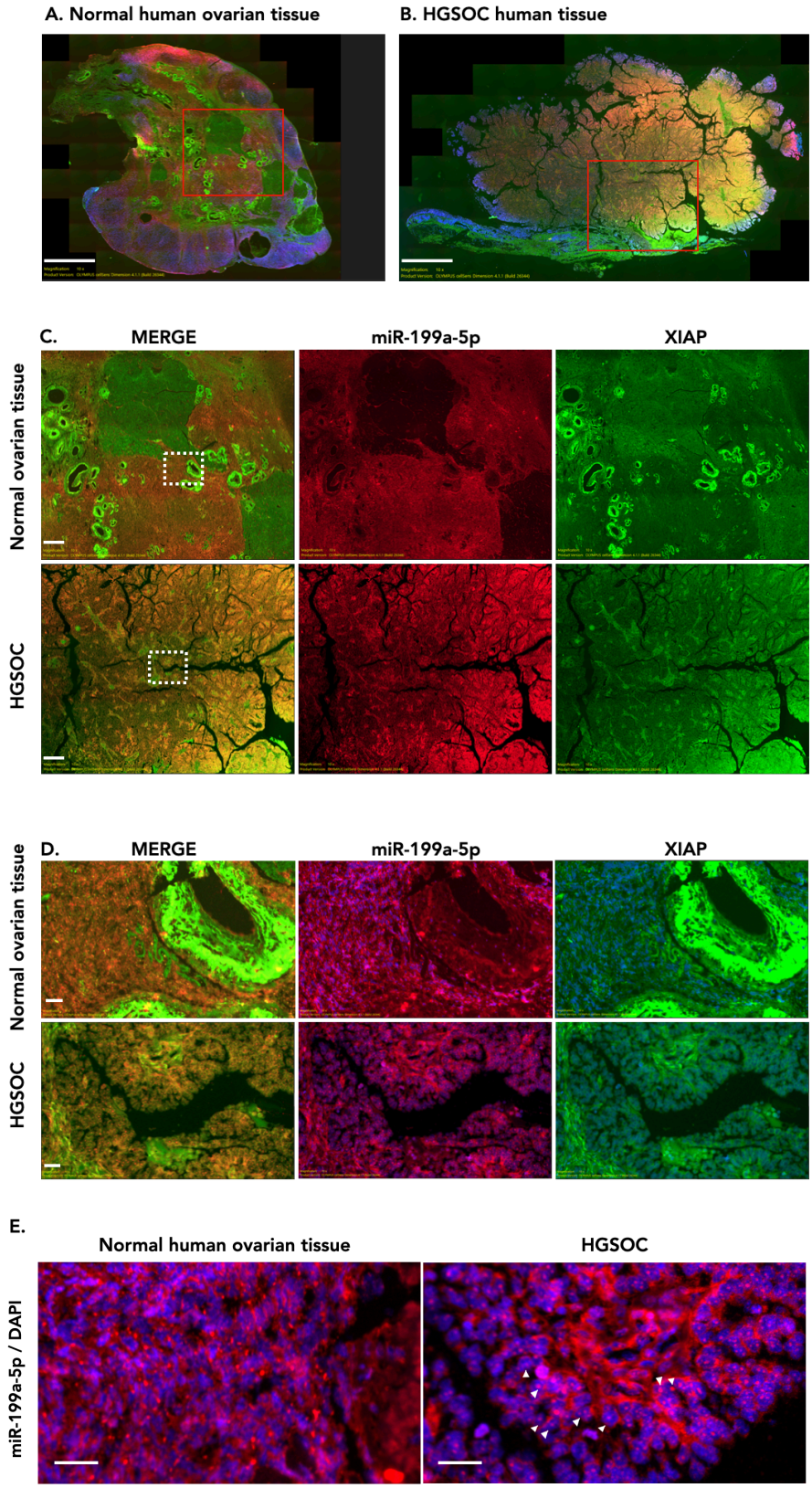

Figure 10. Spatial and subcellular localization patterns of miR-199a-5p and XIAP in normal and malignant ovarian tissue. Representative multiplex fluorescence in situ hybridization (FISH) and immunofluorescence (IF) images of formalin-fixed paraffin-embedded (FFPE) sections from normal human ovarian tissue and high-grade serous ovarian carcinoma (HGSOC). (A–B): Low-magnification overview images from normal ovary (A) and HGSOC (B) showing miR-199a-5p (red), XIAP (green), and nuclei (DAPI, blue). Red boxes indicate areas selected for subsequent magnification. (C–D): Intermediate (C) and high-magnification (D) views of the selected areas in (A) and (B). Each row displays a merged image (left), miR-199a-5p/DAPI (middle), and XIAP/DAPI (right). (E): Digitally zoomed (15×) images of high-magnification fields shown in (D) to better visualize the subcellular distribution of miR-199a-5p in normal ovary (left) and HGSOC (right). Arrows indicate cells exhibiting signal within the nuclear compartment. Scale bars: 100 µm in (A); 50 µm in (B–D); 20 µm in (E).

Colocalization metrics distinguish tumor from control tissues

Quantitative colocalization analysis revealed systematic differences between non-neoplasic and tumor ovarian tissues when assessed using Manders' coefficients and intensity-weighted K indices (Table 3). In non-tumoral samples, miR-199a-5p and XIAP showed a moderate degree of spatial co-localization, with Pearson's correlation

coefficient of 0.464 ± 0.114 and Manders' coefficients M1 = 0.493 ± 0.062 and M2 = 0.510 ± 0.141, indicating partial overlap of both signals within shared pixel regions. Tumor samples showed a consistent increase across these metrics, with Pearson's r rising to 0.541 ± 0.142 and Manders' coefficients increasing to M1=0.574 ± 0.137 (p=0.0247) and M2=0.566 ± 0.191. In contrast, the overlap coefficient remained similarly high in both conditions (control: 0.933 ± 0.035; tumor: 0.926 ± 0.025), indicating an increased fraction of XIAP-associated signal overlapping with miR-199a-5p in malignant tissue.

Variable	Control	Tumor	Test	p_value
Pearson	0.464 ± 0.114	0.541 ± 0.142	Welch t-test	0.214901
M1	0.493 ± 0.062	0.574 ± 0.137	Mann–Whitney U	**0.022018**
M2	0.510 ± 0.141	0.566 ± 0.191	Welch t-test	0.489253
Overlap coefficient	0.933 ± 0.035	0.926 ± 0.025		
CCF_MAX	0.456 ± 0.115	0.534 ± 0.141	Welch t-test	0.211654
CCF_MIN	0.296 ± 0.101	0.371 ± 0.130	Welch t-test	0.181979
K1	0.484 (median)	1.677 (median)	Mann–Whitney U	**0.000022**
K2	1.822 (median)	0.512 (median)	Welch t-test	**0.000100**
FWHM	20.506 (median)	20.235 (median)	Mann–Whitney U	0.660720

Table 3. Intensity-dependent descriptors K1 and K2 further distinguished tumor from control tissues

Consistent with a limited contribution of XIAP to colocalized intensity in non-tumoral samples, control tissues displayed low K1 and higher K2 values (K1 median = 0.484; K2 median = 1.822). In contrast, tumor samples showed a marked inversion of this pattern, with significantly increased K1 (median = 1.677; p = 0.000022) and reduced K2 (median = 0.512; p = 0.000100). Together, these shifts indicate a redistribution of intensity dominance within colocalized pixels, with XIAP contributing more strongly to overlapping regions in tumor tissue compared with controls. Between-group comparisons (tumor vs control) using Mann–Whitney U tests indicated that Manders' M1 and K1 differed most prominently between tumor (n = 9) and control (n = 10) samples. Manders' M1 was significantly higher in tumors (0.574 ± 0.137) than in controls (0.493 ± 0.062; p = 0.0247, Cohen's d = 0.776), while K1 showed a larger effect size (2.035 ± 1.451 vs. 0.498 ± 0.188; p = 0.0003, Cohen's d = 1.530), highlighting K1 as the descriptor with the strongest between-group difference.

DISCUSSION

Ovarian cancer remains a leading cause of gynecological cancer–related mortality, largely due to late-stage diagnosis and the development of resistance to platinum-based chemotherapy[23,24]. A central feature of this resistance is the disruption of apoptotic signaling pathways, including altered regulation of inhibitor of apoptosis proteins such as

XIAP, which suppress caspase activation and attenuate chemotherapy-induced cell death[25]. Furthermore, dysregulation of microRNA expression has been widely implicated in ovarian cancer progression and therapeutic response, reflecting the ability of miRNAs to modulate survival, stress-response, and apoptotic pathways[26,27]. Within this context, miR-199a-5p has been described as a tumor suppressor miRNA with pro-apoptotic functions and reduced expression in ovarian cancer[22,28].

Our laboratory previously validated XIAP as a direct miR-199a-5p target[29], providing a mechanistic rationale to interrogate this axis in ovarian cancer models. In the present study, STarMir predictions using the human V-CLIP model identified an accessible miR-199a-5p site within the XIAP 3'UTR, with LogitProb values above the 0.5 threshold and favorable hybridization energetics that closely matched the murine ortholog ($\Delta G \approx -15.4$ and -15.2 kcal/mol, respectively) (Fig. 1). This degree of cross-species conservation supports the view that the maintenance of this regulatory node is under evolutionary constraint and may contribute to cellular homeostasis. Consistent with this premise, our ovarian cancer data (Figs. 3 and 9) further support that the interaction remains functionally engaged in this cellular background. More broadly, genomic analyses indicate that conserved miRNA binding sites are subject to selective pressure to preserve target-site accessibility[30], a feature we corroborated here via STarMir and RNAfold, highlighting local structural configuration and accessibility as key determinants of miRNA–mRNA coupling[14,16]. Prior to mechanistic analyses of the miR-199a-5p/XIAP axis under cisplatin exposure, the cisplatin-sensitive (A2780) and cisplatin-resistant (A2780cis) lines were benchmarked at baseline to determine whether resistance is accompanied by measurable shifts in miRNA/IAP homeostasis, as reported across ovarian cisplatin-sensitive/resistant model pairs[31,32]. RT-qPCR demonstrated a significant depletion of miR-199a-5p in A2780cis relative to A2780, whereas XIAP mRNA did not differ significantly between lines, consistent with reduced endogenous miR-199a-5p in the resistant state without evidence of transcriptional upregulation of XIAP. However, when resolved at single-cell resolution using combined quantitative FISH/IF, XIAP protein fluorescence intensity showed a trend toward higher values in A2780cis that did not reach statistical significance, whereas miR-199a-5p FISH signal was significantly reduced in the resistant phenotype. Together, these observations underscore that population-averaged bulk readouts (e.g., immunoblotting or bulk transcript measurements) summarize heterogeneous cell populations into a single mean value, whereas single-cell imaging preserves distributional and spatial features that may be relevant for interpreting resistant phenotypes. In line with the framework proposed by Marusyk et al. (2012)[33], such averaging can under-represent biologically meaningful minority cellular states within a sample.

Furthermore, our findings are consistent with established reports across independent ovarian cisplatin-sensitive/resistant model pairs (e.g., OV2008/C13*), where resistance-associated molecular shifts are frequently masked by the averaging effect of bulk quantification. The relevance of the miR-199 family in this context is underscored by studies from Wang et al. (2013)[34] and Feng et al. (2017)[28], which link these family members to platinum response in ovarian cancer. Specifically, the observed depletion of

miR-199a-5p in our resistant model is remarkably consistent with the epigenetic silencing of miR-199b-5p reported by Liu et al. (2014) during the acquisition of cisplatin resistance in paired ovarian systems[35]. By resolving these changes at the single-cell level, we confirm that the miR-199/XIAP axis undergoes a measurable homeostatic shift in the resistant phenotype that population-level assays like qPCR or Western blot fail to fully capture.

In agreement with these predictions and with our prior findings, miR-199a-5p transfection in cisplatin-sensitive human A2780 cells significantly reduced XIAP abundance under basal conditions (Figs. 3 and 9), supporting a negative post-transcriptional contribution of miR-199a-5p to the XIAP/IAP network in this cellular background. Cisplatin exposure also significantly decreased XIAP protein levels (Figs. 5 and 9), consistent with earlier observations in A2780-derived ovarian cancer models linking cisplatin-induced apoptosis to modulation of the XIAP/IAP axis[19,36] and with reports implicating cisplatin-associated XIAP destabilization[37]. No statistically significant miR-199a-5p × cisplatin interaction was detected for XIAP, indicating that miR-199a-5p–mediated repression and cisplatin-driven downregulation contributed largely as independent effects under the experimental conditions tested. This outcome may reflect a reduced dynamic range for detecting further XIAP depletion once basal levels are lowered by miR-199a-5p, thereby limiting detection of an additional cisplatin-dependent decrease[38].

In the resistant setting, miR-199a-5p significantly enhanced cisplatin-induced caspase-3/7 activity (Fig. 7)—indicating a heightened state of apoptotic priming—despite the non-significant trend in late-stage cell death readouts (PI positivity, Fig. 6) in A2780cis cells while exhibiting a paradoxical, interaction-dependent maintenance or increase in XIAP protein levels (Fig. 9; p=0.0057). This dissociation aligns with prior evidence in A2780-derived resistant models where the XIAP-linked response is attenuated compared to sensitive counterparts[19,39]. Such behavior suggests that miR-199a-5p acts as an 'apoptotic priming' agent, sensitizing resistant cells through pleiotropic routes independent of target protein mass, such as the modulation of HIF-1α 28 or the IKKβ/NF-κB pathway [40] . Under cisplatin pressure, stress-dependent remodeling of microRNP function may switch the miRNA output from repression to translational promotion[41,42]. Consequently, XIAP abundance becomes a 'distractor' rather than a reliable indicator of chemosensitivity in the resistant phenotype[43]. These findings emphasize that therapeutic efficacy in miRNA-based strategies should be inferred from the restoration of net apoptotic connectivity rather than single-target readouts[44].

The pro-apoptotic effect of miR-199a-5p was cross-validated through functional fluorescence assays (Fig. 7) and molecular detection of cleaved caspase-3 (Fig. 8). Notably, while imaging resolved a highly significant increase in caspase activity within the resistant population (p=0.0019; Fig. 7B), the corresponding Western blot displayed a supportive but less pronounced trend (Fig. 8C). This recurrent discrepancy between bulk and single-cell readouts reinforces that imaging-based quantification is more sensitive for capturing the early stages of apoptotic engagement in heterogeneous resistant niches. This molecular confirmation, alongside the paradoxical maintenance of XIAP protein

levels (Fig. 9), supports a model where miR-199a-5p restores apoptotic connectivity by lowering the activation threshold of effector caspases, even when the primary target protein remains abundant[44]. Consequently, we asked whether analogous spatial rewiring is detectable in human ovarian tissues where subcellular compartmentalization could further redirect the functional output of the miR-199a-5p/XIAP axis.

Whereas miR-199a-5p repressed XIAP in cisplatin-sensitive A2780 cells, this coupling was lost in A2780cis, indicating context-dependent constraints on miRNA-to-protein output; we therefore examined whether human ovarian tissues exhibit spatial or subcellular organization that could introduce analogous constraints on the miR-199a-5p/XIAP axis. In non-neoplastic ovary, the baseline architecture itself is restrictive: XIAP signal is concentrated within glandular epithelial structures, while miR-199a-5p is comparatively weak and preferentially stromal (Fig. 10A,C–D), a compartmental separation consistent with stromal–epithelial specialization in ovarian tissue and its remodeling during tumorigenesis[45]. In HGSOC, this spatial constraint is attenuated, with miR-199a-5p broadly distributed across epithelial and stromal compartments and partial overlap with XIAP within tumor cellular domains (Fig. 10B–D). Quantitative colocalization analysis revealed a systematic redistribution of intensity dominance within malignant tissue, manifested as a drastic inversion of intensity-weighted indices (K1↑, K2↓) compared to non-neoplastic controls (Table 3). The marked increase in K1—which showed the largest effect size among all descriptors (Cohen's d = 1.530)—identifies a 'regulatory escape signature' in HGSOC (Fig. 10). This class of intensity dominance is effectively captured by descriptors originally proposed by Manders et al. (1993)[46] but is often under-represented when overlap is summarized primarily by correlation-based metrics [47,48]. Biologically, this XIAP-dominant contribution is compatible with cancer contexts where miRNA-mediated repression exhibits threshold-like behavior shaped by relative miRNA/target abundance and competing endogenous pools [38,49,50]. In this framework, the K1 shift reflects a state where XIAP effectively overcomes the repressive threshold of the available miR-199a-5p, allowing target persistence despite spatial coexistence with its regulator [51]. Furthermore, the persistence of XIAP in HGSOC despite increased spatial overlap may be facilitated by tumor-associated 3'UTR remodeling. This hallmark of oncogenic transformation allows transcripts to evade miRNA-mediated control through the loss of repressive elements without altering the protein-coding sequence [52]. Given our identification of a specific binding site at positions 2198–2218 (Fig. 1), such structural shortening provides a compelling genomic mechanism for the 'regulatory escape' observed in our tissue analysis, where XIAP remains abundant despite the presence of its regulator. Within this remodeled overlap architecture, the subcellular distribution of miR-199a-5p becomes particularly relevant, because compartmental mixing alone does not determine whether the miRNA is positioned to engage canonical cytoplasmic mRNA targets. Accordingly, the prominent perinuclear—and in a subset of tumor cells, nuclear—miR-199a-5p enrichment (Fig. 10D–E) is biologically plausible given that mature miRNAs can undergo regulated nuclear import via Importin-8 in an Ago2-dependent manner [53] and that nuclear miRNA activities are increasingly recognized [54], including coupling to RNA-processing machinery such as miR-10b engagement of U6 snRNA with splicing consequences [55].

Importantly, these precedents support the plausibility that subcellular partitioning can reshape regulatory output, but our data remain descriptive at this level and do not establish causality for miR-199a-5p–dependent XIAP persistence in tumor epithelium. In aggregate, the tissue-level remodeling—characterized by stromal–epithelial mixing, the K1 intensity-dominance shift, and miRNA nuclear sequestration—provides a coherent spatial correlate for the chemoresistant phenotype. These findings support a shift in the therapeutic paradigm: miRNA efficacy is determined not by net abundance, but by the spatial connectivity of the regulatory axis [42,44].

BIBLIOGRAPHY

1. Miras, I., Estévez-García, P. & Muñoz-Galván, S. Clinical and molecular features of platinum resistance in ovarian cancer. Crit. Rev. Oncol. Hematol. 201, 104434 (2024).
2. Wagner, V. et al. Circulating extracellular vesicles protein expression for early prediction of platinum-resistance in high-grade serous ovarian cancer. Oncogene 44, 1197–1203 (2025).
3. Denisenko, E. et al. Spatial transcriptomics reveals discrete tumour microenvironments and autocrine loops within ovarian cancer subclones. Nat. Commun. 15, 2860 (2024).
4. Laury, A. R. et al. Opening the Black Box: Spatial Transcriptomics and the Relevance of Artificial Intelligence-Detected Prognostic Regions in High-Grade Serous Carcinoma. Mod. Pathol. Off. J. U. S. Can. Acad. Pathol. Inc 37, 100508 (2024).
5. Nunes, M. et al. Deciphering the Molecular Mechanisms behind Drug Resistance in Ovarian Cancer to Unlock Efficient Treatment Options. Cells 13, 786 (2024).
6. Cetraro, P., Plaza-Diaz, J., MacKenzie, A. & Abadía-Molina, F. A Review of the Current Impact of Inhibitors of Apoptosis Proteins and Their Repression in Cancer. Cancers 14, 1671 (2022).
7. Jiang, C. et al. Molecular mechanisms of cisplatin resistance in ovarian cancer. Genes Dis. 11, 101063 (2024).
8. Atiaa, A. G., Abd E-Kader, S. M. & Ellakwa, D. E.-S. Crosstalk between microRNA and oxidative stress in ovarian cancer: diagnosis, pathogenesis and therapeutic resistance. Med. Oncol. 43, 104 (2025).

9. Hu, X. et al. Recent advances in the functional explorations of nuclear microRNAs. Front. Immunol. 14, 1097491 (2023).
10. Billi, M., De Marinis, E., Gentile, M., Nervi, C. & Grignani, F. Nuclear miRNAs: Gene Regulation Activities. Int. J. Mol. Sci. 25, 6066 (2024).
11. Wang, W. et al. Engineered extracellular vesicles enriched with the miR-214/199a cluster enhance the efficacy of chemotherapy in ovarian cancer. Mol. Oncol. https://doi.org/10.1002/1878-0261.70224 (2026) doi:10.1002/1878-0261.70224.
12. Lian, X.-Y. et al. Ovarian cancer-excreted exosomal miR-199a-5p suppresses tumor metastasis by targeting hypoxia-inducible factor-2α in hypoxia microenvironment. Cancer Commun. 40, 380–385 (2020).
13. Muñoz-Galdeano, T. et al. Identification of a New Role of miR-199a-5p as Factor Implied in Neuronal Damage: Decreasing the Expression of Its Target X-Linked Anti-Apoptotic Protein (XIAP) After SCI. Int. J. Mol. Sci. 25, 12374 (2024).
14. Rennie, W. et al. Sfold Tools for MicroRNA Target Prediction. Methods Mol. Biol. 1970, 31–42 (2019).
15. A Sensitive Alternative for MicroRNA In Situ Hybridizations Using Probes of 2′-O-Methyl RNA + LNA - Martin J. Søe, Trine Møller, Martin Dufva, Kim Holmstrøm, 2011. https://journals.sagepub.com/doi/full/10.1369/0022155411409411.
16. Kertesz, M., Iovino, N., Unnerstall, U., Gaul, U. & Segal, E. The role of site accessibility in microRNA target recognition. Nat. Genet. 39, 1278–1284 (2007).
17. Chi, S. W., Zang, J. B., Mele, A. & Darnell, R. B. Argonaute HITS-CLIP decodes microRNA-mRNA interaction maps. Nature 460, 479–486 (2009).
18. Hafner, M. et al. Transcriptome-wide identification of RNA-binding protein and microRNA target sites by PAR-CLIP. Cell 141, 129–141 (2010).
19. Asselin, E., Mills, G. B. & Tsang, B. K. XIAP regulates Akt activity and caspase-3-dependent cleavage during cisplatin-induced apoptosis in human ovarian epithelial cancer cells. Cancer Res. 61, 1862–1868 (2001).
20. Lian, X.-Y. et al. Ovarian cancer-excreted exosomal miR-199a-5p suppresses tumor metastasis by targeting hypoxia-inducible factor-2α in hypoxia microenvironment. Cancer Commun. 40, 380–385 (2020).

21. Liu, X., Yao, B. & Wu, Z. miRNA-199a-5p suppresses proliferation and invasion by directly targeting NF-κB1 in human ovarian cancer cells. Oncol. Lett. 16, 4543–4550 (2018).
22. Kinose, Y. et al. The hypoxia-related microRNA miR-199a-3p displays tumor suppressor functions in ovarian carcinoma. Oncotarget 6, 11342–11356 (2015).
23. Sung, H. et al. Global Cancer Statistics 2020: GLOBOCAN Estimates of Incidence and Mortality Worldwide for 36 Cancers in 185 Countries. CA. Cancer J. Clin. 71, 209–249 (2021).
24. Lheureux, S., Gourley, C., Vergote, I. & Oza, A. M. Epithelial ovarian cancer. Lancet 393, 1240–1253 (2019).
25. Cremona, M. et al. BRCA mutations lead to XIAP overexpression and sensitise ovarian cancer to inhibitor of apoptosis (IAP) family inhibitors. Br. J. Cancer 127, 488–499 (2022).
26. Ghafouri-Fard, S., Dashti, S. & Taheri, M. PCAT1: An oncogenic lncRNA in diverse cancers and a putative therapeutic target. Exp. Mol. Pathol. 114, 104429 (2020).
27. Kandettu, A. et al. Deregulated miRNA clusters in ovarian cancer: Imperative implications in personalized medicine. Genes Dis. 9, 1443–1465 (2022).
28. Feng, X. et al. miR-199a modulates cisplatin resistance in ovarian cancer by targeting Hif1α. OncoTargets Ther. 10, 5899–5906 (2017).
29. Muñoz-Galdeano, T. et al. Identification of a New Role of miR-199a-5p as Factor Implied in Neuronal Damage: Decreasing the Expression of Its Target X-Linked Anti-Apoptotic Protein (XIAP) After SCI. Int. J. Mol. Sci. 25, 12374 (2024).
30. Most mammalian mRNAs are conserved targets of microRNAs - PubMed. https://pubmed.ncbi.nlm.nih.gov/18955434/.
31. Kumar, S. et al. MicroRNA signature of cis-platin resistant vs. cis-platin sensitive ovarian cancer cell lines. J. Ovarian Res. 4, 17 (2011).
32. Zhang, X., Huang, L., Zhao, Y. & Tan, W. Downregulation of miR-130a contributes to cisplatin resistance in ovarian cancer cells by targeting X-linked inhibitor of apoptosis (XIAP) directly. Acta Biochim. Biophys. Sin. 45, 995–1001 (2013).

33. Marusyk, A., Almendro, V. & Polyak, K. Intra-tumour heterogeneity: a looking glass for cancer? Nat. Rev. Cancer 12, 323–334 (2012).
34. Wang, Z. et al. microRNA-199a is able to reverse cisplatin resistance in human ovarian cancer cells through the inhibition of mammalian target of rapamycin. Oncol. Lett. 6, 789–794 (2013).
35. Liu, M. X. et al. Epigenetic silencing of microRNA-199b-5p is associated with acquired chemoresistance via activation of JAG1-Notch1 signaling in ovarian cancer. Oncotarget 5, 944–958 (2014).
36. Li, J. et al. Human Ovarian Cancer and Cisplatin Resistance: Possible Role of Inhibitor of Apoptosis Proteins*This work was supported by grants from the Canadian Institutes of Health Research (MOP-15691), the University of Ottawa-Industry Grants Program, and the Ottawa Civic Hospital Foundation. Endocrinology 142, 370–380 (2001).
37. He, X., Khurana, A., Maguire, J. L., Chien, J. & Shridhar, V. HtrA1 sensitizes ovarian cancer cells to cisplatin-induced cytotoxicity by targeting XIAP for degradation. Int. J. Cancer 130, 1029–1035 (2012).
38. Mukherji, S. et al. MicroRNAs can generate thresholds in target gene expression. Nat. Genet. 43, 854–859 (2011).
39. Ma, J., Chen, B. & Xin, X. XIAP gene downregulation by small interfering RNA inhibits proliferation, induces apoptosis, and reverses the cisplatin resistance of ovarian carcinoma. Eur. J. Obstet. Gynecol. Reprod. Biol. 146, 222–226 (2009).
40. Chen, R. et al. Regulation of IKKβ by miR-199a affects NF-κB activity in ovarian cancer cells. Oncogene 27, 4712–4723 (2008).
41. Bhattacharyya, S. N., Habermacher, R., Martine, U., Closs, E. I. & Filipowicz, W. Relief of microRNA-mediated translational repression in human cells subjected to stress. Cell 125, 1111–1124 (2006).
42. Vasudevan, S., Tong, Y. & Steitz, J. A. Switching from repression to activation: microRNAs can up-regulate translation. Science 318, 1931–1934 (2007).
43. Mendell, J. T. & Olson, E. N. MicroRNAs in stress signaling and human disease. Cell 148, 1172–1187 (2012).

44. Rupaimoole, R. & Slack, F. J. MicroRNA therapeutics: towards a new era for the management of cancer and other diseases. Nat. Rev. Drug Discov. 16, 203–222 (2017).
45. Mitra, A. K. et al. MicroRNAs reprogram normal fibroblasts into cancer-associated fibroblasts in ovarian cancer. Cancer Discov. 2, 1100–1108 (2012).
46. Manders, E. M. M., Verbeek, F. J. & Aten, J. A. Measurement of co-localization of objects in dual-colour confocal images. J. Microsc. 169, 375–382 (1993).
47. Bolte, S. & Cordelières, F. P. A guided tour into subcellular colocalization analysis in light microscopy. J. Microsc. 224, 213–232 (2006).
48. Dunn, K. W., Kamocka, M. M. & McDonald, J. H. A practical guide to evaluating colocalization in biological microscopy. Am. J. Physiol. - Cell Physiol. 300, C723–C742 (2011).
49. Denzler, R. et al. Impact of MicroRNA Levels, Target-Site Complementarity, and Cooperativity on Competing Endogenous RNA-Regulated Gene Expression. Mol. Cell 64, 565–579 (2016).
50. Salmena, L., Poliseno, L., Tay, Y., Kats, L. & Pandolfi, P. P. A ceRNA hypothesis: the Rosetta Stone of a hidden RNA language? Cell 146, 353–358 (2011).
51. Zinchuk, V., Zinchuk, O. & Okada, T. Quantitative colocalization analysis of multicolor confocal immunofluorescence microscopy images: pushing pixels to explore biological phenomena. Acta Histochem. Cytochem. 40, 101–111 (2007).
52. Mayr, C. & Bartel, D. P. Widespread shortening of 3'UTRs by alternative cleavage and polyadenylation activates oncogenes in cancer cells. Cell 138, 673–684 (2009).
53. Wei, Y., Li, L., Wang, D., Zhang, C.-Y. & Zen, K. Importin 8 regulates the transport of mature microRNAs into the cell nucleus. J. Biol. Chem. 289, 10270–10275 (2014).
54. Catalanotto, C., Cogoni, C. & Zardo, G. MicroRNA in Control of Gene Expression: An Overview of Nuclear Functions. Int. J. Mol. Sci. 17, 1712 (2016).
55. El Fatimy, R. et al. A nuclear function for an oncogenic microRNA as a modulator of snRNA and splicing. Mol. Cancer 21, 17 (2022).

ETHICAL APPROVEMENT

The present study was approved by the Committee for the Review of Human Research at the Complejo Hospitalario de Toledo (CEIM n° 968). All participants provided written informed consent before inclusion. This study was performed according to the principles of the Declaration of Helsinki and the Code of Federal Regulation regarding Protection of Human Subjects.

FUNDINGS

This research was funded by grants from the Fundación Eurocaja Rural "Ayudas Sociales" 2022 y 2025 and the Council of Education, Culture, and Sports of the Regional Government of Castilla La Mancha (Spain) and Co-financed by the European Union (FEDER) "A way to make Europe" (project references SBPLY/17/000376 and SBPLY/21/180501/000097).

ACKNOWLEDGEMENTS

We are deeply grateful to the exceptional support provided by Dr. J.A. Rodriguez Alfaro and Dr. J. Mazarío at the Microscopy and Image Analysis Core Facilities of the National Paraplegic Hospital, Toledo, whose expertise greatly enhanced the imaging and analytical aspects of this study. Additionally, we would like to express our appreciation to the Fundación Eurocaja Rural and to the Consejería de Sanidad de Castilla La Mancha and SESCAM for their support.